Article

Barcoded viral tracing identifies immunosuppressive astrocyte–glioma interactions

https://doi.org/10.1038/s41586-025-09191-9

Received: 15 April 2024

Accepted: 23 May 2025

Published online: 25 June 2025

Check for updates

Brian M. Andersen[1,2,14], Camilo Faust Akl[1,3,14], Michael A. Wheeler[1,4,5], Zhaorong Li[1], Martin Diebold[6], Michael Kilian[1], Joseph M. Rone[1,5], Aditya Misra[5,7,8], Jessica E. Kenison[1], Joon-Hyuk Lee[1], Hong-Gyun Lee[1], Carolina M. Polonio[1], David Merrell[4], Jakob H. Weiss[4], Lillie Godinez[1], Gavin Piester[1], Tomer Illouz[1], Jessica J. Ye[1], Arianna Ghia[1], Jazmin Martinez[1], Elizabeth N. Chung[1], Lena Srun[1], Daniel Farrenkopf[1], Lucas E. Flausino[1], Anton M. Schüle[1], Liliana M. Sanmarco[1], Federico Giovannoni[1], Luca Fehrenbacher[6], Marc Charabati[1], Cristina Gutiérrez-Vázquez[1], Margaret M. Cusick[8,9], Prem S. Prabhakar[8,9], Connor C. Bossi[8,9], Emily Lapinskas[8,9], Roni Nowarski[1,4,5], Gad Getz[4,10], Keith L. Ligon[8,9], Marco Prinz[6,11], E. Antonio Chiocca[12], David A. Reardon[13] & Francisco J. Quintana[1,4,5] ✉

Glioblastoma (GBM) is the most lethal primary brain malignancy[1]. Immunosuppression in the GBM tumour microenvironment (TME) is an important barrier to immune-targeted therapies, but our understanding of the mechanisms of immune regulation in the GBM TME is limited[2]. Here we describe a viral barcode interaction-tracing approach[3] to analyse TME cell–cell communication in GBM clinical samples and preclinical models at single-cell resolution. We combine it with single-cell and bulk RNA-sequencing analyses, human organotypic GBM cultures, in vivo cell-specific CRISPR–Cas9-driven genetic perturbations as well as human and mouse experimental systems to identify an annexin A1–formyl peptide receptor 1 (ANXA1–FPR1) bidirectional astrocyte–GBM communication pathway that limits tumour-specific immunity. FPR1 inhibits immunogenic necroptosis in tumour cells, and ANXA1 suppresses NF-κB and inflammasome activation in astrocytes. ANXA1 expression in astrocytes and FPR1 expression in cancer cells are associated with poor outcomes in individuals with GBM. The inactivation of astrocyte–glioma ANXA1–FPR1 signalling enhanced dendritic cell, T cell and macrophage responses, increasing infiltration by tumour-specific $CD8^+$ T cells and limiting T cell exhaustion. In summary, we have developed a method to analyse TME cell–cell interactions at single-cell resolution in clinical samples and preclinical models, and used it to identify bidirectional astrocyte–GBM communication through ANXA1–FPR1 as a driver of immune evasion and tumour progression.

GBM is an aggressive form of brain cancer with a five-year survival rate of less than 10% (ref. 1). The lack of effective therapies leaves patients in dire need of effective options, despite undergoing surgery, radiation and chemotherapy[1]. Although immunotherapies such as T cell checkpoint blockade have revolutionized treatment for many malignancies, immunotherapy has been unsuccessful in GBM[1]. The immune-mediated recognition and targeting of GBM is limited by heterogeneity within tumours and between patients, as well as by a complex TME, in which the drivers of immunosuppression are poorly understood[2].

Cell–cell interactions in the GBM TME have central roles in establishing an immunosuppressive microenvironment that limits tumour-specific immune responses. For instance, tumour-associated macrophages (TAMs) in the TME interact with T cells[4–6] and cancer cells[5,7,8] to promote cancer progression. Furthermore, astrocyte interactions with immune cells regulate inflammation in autoimmune and neurodegenerative diseases[9,10], but their contributions to GBM TME immunosuppression are not well understood. Indeed, the systematic investigation of TME cell–cell interactions that promote GBM immune evasion has been limited by a lack of tools for unbiased analysis in clinical samples and experimental models at single-cell resolution.

Here we describe the development of a viral barcode interaction-tracing approach to study TME cell–cell interactions in GBM clinical

[1]Ann Romney Center for Neurologic Diseases, Brigham and Women's Hospital, Harvard Medical School, Boston, MA, USA. [2]Department of Neurology, Veterans Affairs Medical Center, Harvard Medical School, Jamaica Plain, MA, USA. [3]Faculty of Biology, University of Freiburg, Freiburg, Germany. [4]Broad Institute of MIT and Harvard, Cambridge, MA, USA. [5]The Gene Lay Institute of Immunology and Inflammation, Brigham and Women's Hospital, Harvard Medical School, Boston, MA, USA. [6]Institute of Neuropathology, Faculty of Medicine, University of Freiburg, Freiburg, Germany. [7]Harvard-MIT Health Sciences and Technology, Massachusetts Institute of Technology, Cambridge, MA, USA. [8]Department of Pathology, Dana-Farber Cancer Institute, Harvard Medical School, Boston, MA, USA. [9]Department of Pathology, Brigham & Women's Hospital, Harvard Medical School, Boston, MA, USA. [10]Department of Pathology and Krantz Family Center for Cancer Research, Harvard Medical School, Massachusetts General Hospital, Boston, MA, USA. [11]Signalling Research Centres BIOSS and CIBSS, University of Freiburg, Freiburg, Germany. [12]Department of Neurosurgery, Brigham and Women's Hospital, Harvard Medical School, Boston, MA, USA. [13]Department of Medical Oncology, Dana-Farber Cancer Institute, Harvard Medical School, Boston, MA, USA. [14]These authors contributed equally: Brian M. Andersen, Camilo Faust Akl. ✉e-mail: fquintana@rics.bwh.harvard.edu

samples and preclinical models with single-cell resolution. Using this innovative approach, we have identified a bidirectional communication pathway involving *ANXA1* expressed in astrocytes and its receptor *FPR1* expressed in GBM cells and found that it limits tumour-specific immune responses. In summary, we have developed a new approach for the investigation of cellular interactions in the TME and were able to identify mechanisms of disease pathogenesis and candidate therapeutic targets in GBM.

Sequencing and viral barcoding of GBM tissue

To study astrocyte functions in GBM, we first analysed single-cell RNA sequencing (scRNA-seq) data from clinical GBM specimens[11], identifying malignant cells by copy-number variation analysis of chromosome 7 gain and chromosome 10 loss[11,12] (Fig. 1a). We next used a combination of gene expression and downstream pathway activation to rank differentially expressed genes (DEGs) in non-malignant astrocytes by their biological relevance. *ANXA1* (which encodes annexin A1) ranked highest among recurrence- and disease-associated DEGs (Fig. 1a,b, Extended Data Fig. 1a and Supplementary Data 1 and 2). Indeed, *ANXA1* transcripts were enriched in astrocytes from individuals with GBM compared with non-diseased astrocytes, as well as in astrocytes from individuals with GBM with accelerated recurrence of less than 12 months (Fig. 1c and Extended Data Fig. 1a–d). To validate these findings, we used multiplex immunofluorescence microscopy to analyse two independent cohorts of patients with GBM (Supplementary Data 3), using *OLIG2* or *SOX2* expression to identify tumour cells[13,14] (Extended Data Fig. 1e,f). We detected increased *ANXA1* expression in astrocytes surrounding areas of high SOX2$^+$ or OLIG2$^+$ tumour cellular density (Fig. 1d–f and Extended Data Fig. 1g–j); GBM cells expressed lower levels of *ANXA1* (Extended Data Fig. 1g,j). Furthermore, spatial transcriptomics datasets[15] showed *ANXA1* expression to be highly enriched in non-malignant astrocytes[16], which are most abundant at the infiltrating tumour zone of GBM (Extended Data Fig. 1k,l). These findings indicate that *ANXA1* expression in astrocytes is linked to TME regions where tumour cells are likely to remain after surgery and are associated with worse outcomes in GBM.

We next adapted our method for in vivo labelling of interacting cells with barcoded mCherry in a process called rabies barcode interaction detection followed by scRNA-seq (RABID-seq[3]), using glycoprotein-deficient pseudotyped rabies virus to detect interactions between ANXA1$^+$ astrocytes and other cells in GBM surgical specimens. First, we established organotypic slice cultures from surgical specimens obtained from three patients with recurrent GBM (Supplementary Table 1). In RABID-seq, the uniquely barcoded glycoprotein-deficient rabies virus (RabΔG) is pseudotyped with EnvA to limit initial infection to cells expressing TVA; replication is limited to cells expressing glycoprotein G that are required for envelope formation[3]. Thus, we used a lentiviral vector to transduce the genes encoding TVA and glycoprotein G under the control of the EF1α promoter in GBM organotypic slice cultures, enabling initial RabΔG entry into any cell type (Fig. 1g and Extended Data Fig. 1m–s). Indeed, we used immunofluorescence to detect infection by the TVA/G-expressing lentivirus and RabΔG (Extended Data Fig. 2a–z). Five days after lentiviral transduction, we infected the cultures with RabΔG, and five days later we isolated mCherry$^+$ cells by flow-cytometry sorting; mCherry$^+$ cells were then analysed by scRNA-seq to detect transcriptomes and shared barcodes indicative of cell–cell interactions (Fig. 1g).

We detected barcodes shared between tumour cells and macrophages, astrocytes, endothelial cells and neurons, but astrocytes shared the greatest number of barcodes with malignant cells (Fig. 1h,i and Extended Data Fig. 1m–s). Of note, lower than expected numbers of oligodendrocytes and neurons are consistent with previous reports using similar tissue-dissociation methods followed by flow-cytometry sorting[17]. Notably, astrocytes expressing the *ANXA1* gene signature shared numerous barcodes with malignant cells indicative of abundant interactions (Fig. 1i) and were enriched for several immunosuppressive genes and pathways, such as LGALS1, PD-1–PD-L1, TME, TGFβ and STAT3 signalling (Fig. 1j,k and Supplementary Data 4 and 5). In summary, we developed patient-tissue RABID-seq (ptRABID-seq), a barcoding approach to study TME cell–cell interactions in tissue from patients with GBM, which identified ANXA1$^+$ astrocytes that interact with GBM cells and show an immunosuppressive phenotype.

Tumour-anchored RABID-seq of mouse glioma

We next investigated astrocyte–glioma interactions in vivo using the GL261 orthotopic murine glioma model in syngeneic B6 wild-type mice. To develop a RABID-seq approach in which RabΔG first infects tumour cells and then spreads to other interacting cells in the TME in vivo (tumour-anchored RABID-seq; taRABID-seq), we engineered mouse GL261 cells to express glycoprotein G and the EnvA receptor TVA. We implanted wild-type B6 mice intracranially with GL261 cells expressing glycoprotein G and TVA, and after confirmation of tumour growth, we injected barcoded RabΔG at the same site (Fig. 2a). One week after RabΔG injection, virus-infected mCherry$^+$ GL261 and interacting non-malignant cells, including astrocytes, were sorted by flow cytometry and analysed by scRNA-seq to detect cell transcriptomes and shared barcodes (Fig. 2b,c and Extended Data Figs. 3a–p and 4a–c). The analysis of astrocyte–tumour interaction networks by taRABID-seq detected abundant connections between GL261 cells (distinguished by GFP expression) and astrocytes enriched for the ANXA1 signature (Fig. 2d and Extended Data Fig. 4d). We detected no differences in ANXA1 signature expression in astrocytes isolated 14 or 21 days after tumour implantation (Extended Data Fig. 4e). Moreover, ANXA1 signature-positive astrocytes connected to GL261 cells displayed decreased expression of NLRP3 inflammasome components (*Nlrp3* and *Nek1*) and a concomitant upregulation of anti-inflammatory molecules (*Tgfbr1*, *Entpd1*, *Il10rb*, *Havcr2* and *Vsir*) and signalling pathways (IL-10, TGFβ, STAT3 and arginase signalling) when compared with ANXA1$^+$ astrocytes not connected to cancer cells (Fig. 2e and Supplementary Data 6). Reciprocally, GL261 cells interacting with astrocytes displaying an ANXA1 signature exhibited upregulation of PD-1–PD-L1 signalling and downregulation of neuroinflammatory signalling and necroptosis, an immunogenic form of cell death that activates T cell responses[18] (Fig. 2f and Supplementary Data 7). Indeed, multiple suppressors of necroptosis (*Traf2*, *Cflar*, *Ripk1* and *Hmox1*) were upregulated, whereas necroptosis drivers were downregulated (*Cyld* and *Pcbp2*)[19]. Hence, our RABID-seq analyses of clinical and pre-clinical samples indicate that ANXA1$^+$ astrocytes and glioma cells participate in bidirectional immunosuppressive interactions.

We also identified other candidate mediators of GBM cell–cell interactions by taRABID-seq. When comparing DEGs between connected and non-connected tumour cell–astrocyte pairs in taRABID-seq, we detected an enrichment of *Axl* in connected GL261 cells interacting with astrocytes (Extended Data Fig. 4f). Indeed, *Axl* inactivation in GL261 cells extended survival in tumour-bearing mice (Extended Data Fig. 4g). Furthermore, tumour cells interacting with TAMs were enriched for known (*Cd47* and *Pdcd1lg2*) and new candidate regulators of pathogenic GBM–TAM interactions, such as *Cd38* (ref. 20), *Cd93* (ref. 21), *Tmem60* (ref. 22), *Asb3* (ref. 23), *Btf3l4* (ref. 24) and *S100a10* (ref. 25) (Extended Data Fig. 4h); these molecules have been associated with worsened prognosis and implicated in immunosuppression, but they remain mechanistically unexplored in GBM.

FPR1 in GBM is linked to poor prognosis

ANXA1 is an agonist of formyl peptide receptors (FPRs)[26]. We detected *FPR1* expression in our GBM scRNA-seq dataset[11]; *FPR2* and *FPR3* showed lower expression (Extended Data Fig. 5a–e). We validated FPR1 protein

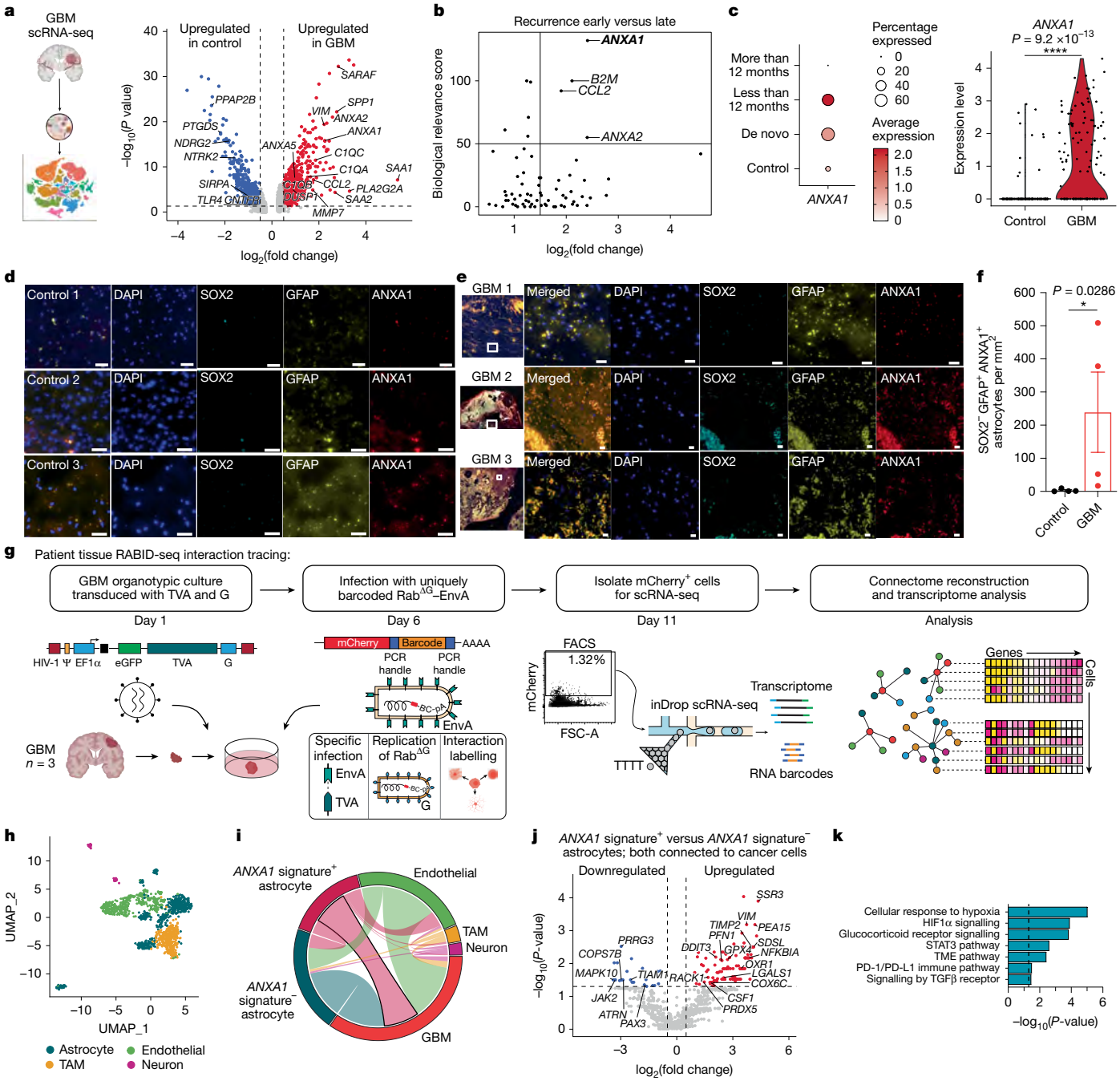

Fig. 1 | Patient-tissue RABID-seq identifies ANXA1⁺ astrocytes in human GBM. a, Dataset schematic and volcano plot of DEGs detected in astrocytes by scRNA-seq in a GBM cohort[11]; $n = 392$ astrocytes. **b**, Biological relevance score of astrocyte DEGs from early- and late-recurring tumours, calculated according to the differential expression and number of pathways affected by each gene. **c**, Astrocyte *ANXA1* expression in scRNA-seq GBM dataset showing time to recurrence. **d**,**e**, Representative images of immunofluorescence analysis of three control (**d**) and three GBM tumours (**e**) at the infiltrating tumour zone displaying *ANXA1* expression in astrocytes. Scale bars, 25 µm. **f**, Quantification of *ANXA1* expression in non-malignant astrocytes ($n = 4$ control non-diseased brain specimens; $n = 4$ GBM specimens). In total, $n = 11{,}505$ GBM-associated astrocytes and $n = 7{,}755$ control astrocytes were quantified. Data show mean ± s.e.m. and *P* values calculated using unpaired two-sided Mann–Whitney *U*-test. **g**, Schematic of ptRABID-seq to study clinical samples. **h**, UMAP plot of non-malignant cells from organotypic GBM cultures analysed by ptRABID-seq ($n = 1{,}520$ cells). **i**, Connectome captured by ptRABID-seq. Bands represent connections between two cell types; band width corresponds to the number of connections detected. ANXA1 signature-positive astrocytes are highlighted in the astrocyte–GBM band ($n = 219$ tumour cells and $n = 149$ astrocytes). **j**, DEGs between ANXA1 signature-positive astrocytes and *ANXA1* signature-negative astrocytes connected to GBM cells. **k**, Ingenuity pathway analysis of the DEGs shown in **j**. Illustrations in **a** and **g** created in BioRender (Lee, J. https://BioRender.com/0bkvepw; 2025).

expression in GBM cells in a cohort of EGFRvIII⁺ patients (Fig. 3a,b and Extended Data Fig. 5f); FPR2 and FPR3 were expressed at lower levels. We therefore studied the role of FPR1 in GBM.

We evaluated the correlation between *FPR1* expression and disease outcomes in GBM. FPR1 protein expression by GBM cells was inversely correlated with survival (Fig. 3b and Supplementary Data 3). *FPR1* expression was also higher in individuals with GBM with accelerated recurrence (Fig. 3c). Furthermore, a transcriptional signature of *FPR1* signalling in GBM cells derived from our scRNA-seq dataset was associated with shorter survival time in a multivariate analysis of GBM cohorts

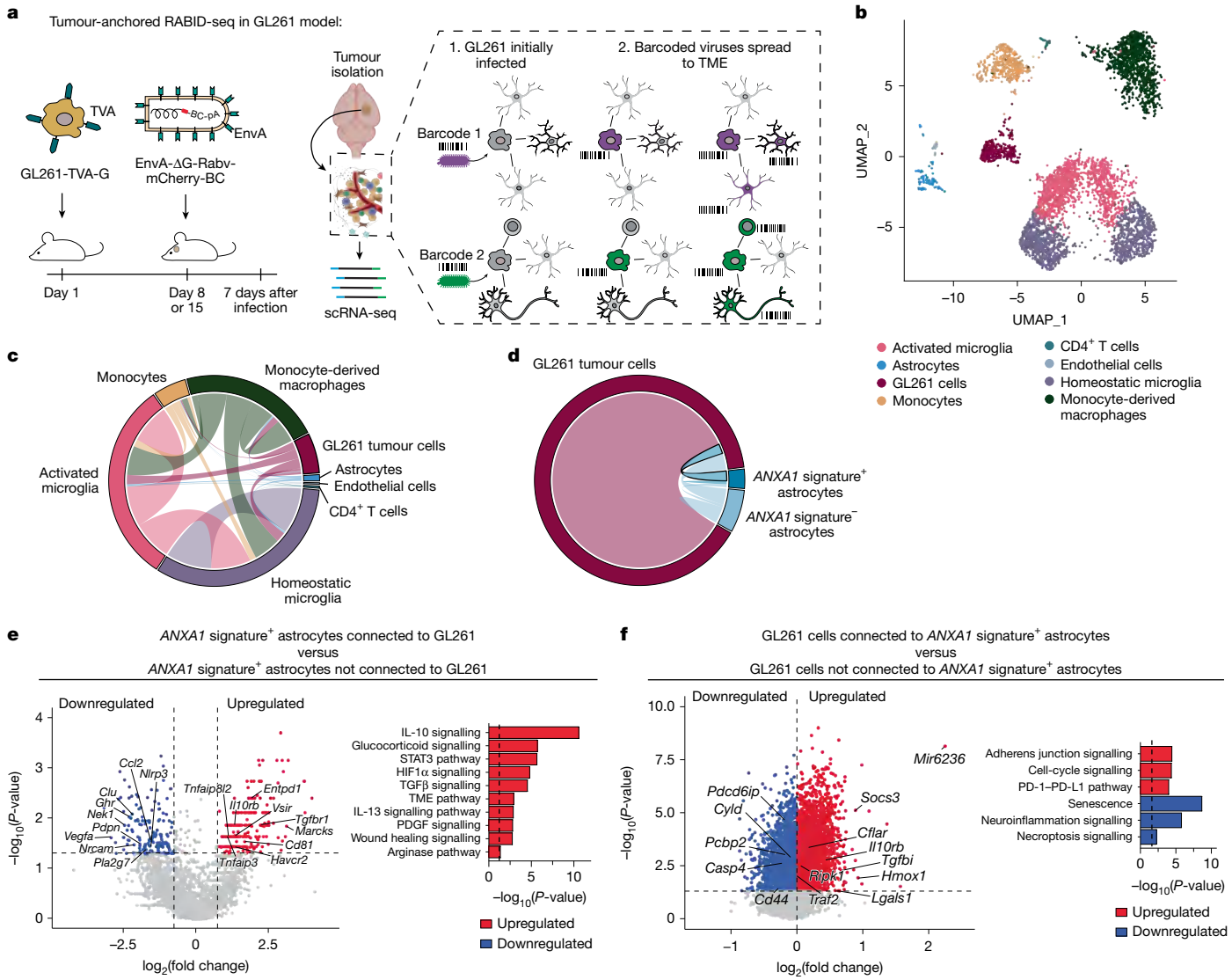

Fig. 2 | Tumour-anchored RABID-seq detects astrocyte–glioma communication. a, Schematic of taRABID-seq to study the TME. **b**, UMAP of cells analysed by taRABID-seq ($n = 6$ mice, $n = 21{,}189$ cells). **c**, Circos plot showing connectome captured by taRABID-seq. **d**, Circos plot of astrocyte–GL261 connections divided by ANXA1 signature expression ($n = 307$ tumour cells, $n = 83$ astrocytes). **e**, Volcano plot and ingenuity pathway analysis of DEGs in ANXA1 signature-positive astrocytes comparing astrocytes connected to GL261 cells with astrocytes not connected to GL261 cells. **f**, Volcano plot and ingenuity pathway analysis of DEGs comparing GL261 cells connected to ANXA1 signature-positive astrocytes with GL261 cells that are not connected. Illustrations in **a** created in BioRender (Lee, J. https://BioRender.com/0bkvepw; 2025).

from The Cancer Genome Atlas (TCGA) and Glioma Longitudinal Analysis (GLASS) datasets (Fig. 3d and Supplementary Data 8).

To further evaluate the functional relevance of FPR1 expression in glioma cells, we inactivated *Fpr1* in mouse GL261 cells using the CRISPR–Cas9 system and a specific targeting guide RNA (gRNA), using a random-sequence gRNA and a gRNA targeting *Fpr2* as controls (Fig. 3e and Extended Data Fig. 5g). *Fpr1* inactivation did not affect GL261 cell proliferation (Extended Data Fig. 5h) but extended survival after intracranial implantation of GL261 and CT-2A tumours (Fig. 3f and Extended Data Fig. 5i). Notably, inactivation of the *Fpr1*-related gene *Fpr2* in GL261 cells had no effect on survival (Extended Data Fig. 5j). Moreover, there was no survival benefit from *Fpr1* inactivation in GL261 cells implanted into *Rag2*-deficient mice (Extended Data Fig. 5k). Collectively, these findings indicate that the ANXA1 receptor FPR1 in tumour cells contributes to GBM pathology by modulating the adaptive immune response against the tumour.

To investigate the role of intratumoral spatial heterogeneity in FPR1 expression in GBM cells, we evaluated the correlation of FPR1 expression with recently defined glioblastoma cell layers and spatial niches[16,27]. FPR1 expression was most highly correlated with the immune hub layer (Extended Data Fig. 5l) and with tumour cells displaying a mesenchymal-like cellular state (Extended Data Fig. 5m). Notably, the immune hub layer is adjacent to the outer margins of the tumour[16], which include the infiltrating tumour zone[27]. Indeed, FPR1 and ANXA1 were most highly co-expressed at the infiltrating tumour zone[27] (Extended Data Fig. 5n). These data, in combination with in vitro evidence that *Fpr1* inactivation impairs the migratory capacity of glioma cells (Extended Data Fig. 5o), indicate that ANXA1–FPR1 interactions contribute to immunosuppression as GBM cells migrate from the tumour core to more distant sites.

FPR1 suppresses GBM cell necroptosis

To further evaluate the role of FPR1 in glioma, we analysed RNA-seq control or *Fpr1*-inactivated GL261 cells 24 days after implantation in wild-type B6 mice (Fig. 3g). *Fpr1* inactivation resulted in increased

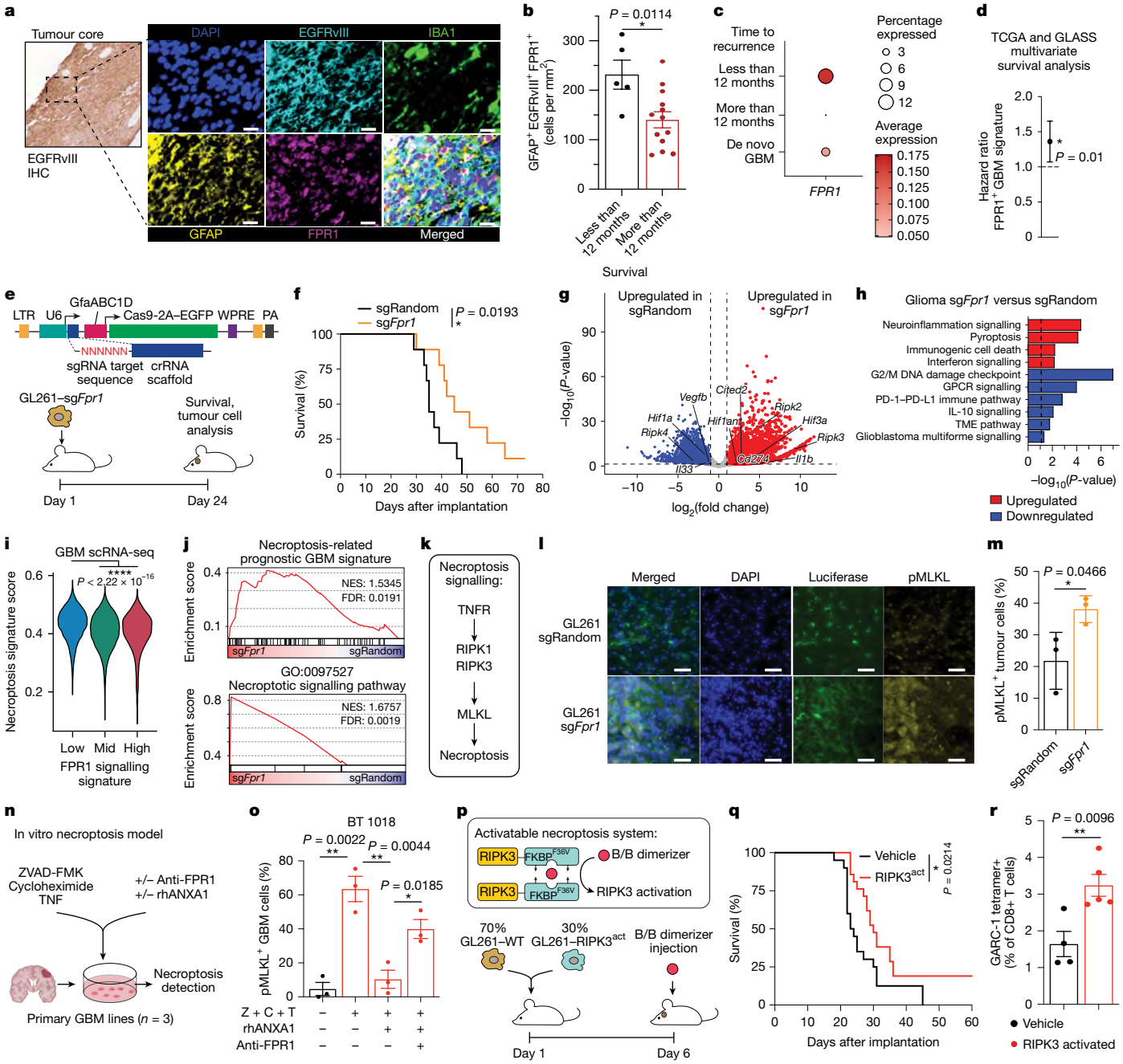

Fig. 3 | FPR1 expression in GBM suppresses necroptosis and is associated with worse prognosis. a,**b**, Representative images (**a**) and analysis (**b**) of FPR1 protein levels in GBM cells from patients surviving less than 12 months or 12 months or more ($n = 18$ patients). **c**, GBM *FPR1* expression by time to recurrence in GBM scRNA-seq[11] ($n = 25$ patients). **d**, Multivariate survival analysis of *FPR1* signature in $n = 141$ individuals with GBM from the TCGA or GLASS (hazard ratio, 1.36 with 95% confidence interval (1.07–1.65); Cox proportional hazards model). **e**, Schematic of *Fpr1* inactivation in GL261 cells. crRNA, CRISPR RNA. **f**, Kaplan–Meier plot of mice bearing GL261 harbouring *Fpr1* or random control sequence gRNA ($n = 9$ mice each, log rank test). **g**,**h**, RNA-seq of GL261 cells after *Fpr1* (sg*Fpr1*) or control (sgRandom) inactivation 24 days after implantation, showing volcano plot (**g**) and pathway analysis (**h**) ($n = 4$ mice each). **i**, Violin plot of necroptosis and FPR signalling signatures in cells from individuals with GBM[11,28]. **j**, Published necroptosis-related prognostic GBM signature[28] and necroptosis signalling signature (GOBP_M24779) applied to RNA-seq of GL261 after *Fpr1* (sg*Fpr1*) or control (sgRandom) inactivation. **k**, Necroptosis pathway schematic. **l**,**m**, Immunofluorescence microscopy (**l**) and quantification (**m**) of pMLKL in GL261 sg*Fpr1*-implanted mice ($n = 3$ mice per group, two-sided unpaired *t*-test). **n**, Design of in vitro studies using primary human GBM isolates treated with ZVAD-FMK (Z), cycloheximide (C) and TNF (T) to induce necroptosis. **o**, pMLKL in one human GBM isolate after necroptosis induction with recombinant human ANXA1 and/or an FPR1-neutralizing antibody (one dot per well with $n = 3$ wells). **p**, Design of the necroptosis system using the GL261–RIPK3^{act} model followed by in vivo activation by B/B homodimerizer (also known as AP20187) administration. **q**, Kaplan–Meier plot of GL261 cells expressing small-molecule-activatable RIPK3 ($n = 20$ mice each; log-rank test). **r**, Intratumoral GL261 GARC-1-specific CD8$^+$ T cells; *P* value calculated using an unpaired two-tailed *t*-test. Graphs in **f**,**m**,**o**,**q** and **r** represent one of three independent replicate experiments and *P* values were from two-sided unpaired *t*-tests in **b**,**i**,**m**,**o** and **r**. $^{****}P < 0.0001$, $^{**}P < 0.01$, $^{*}P < 0.02$. Data are mean ± s.e.m. in **b**,**m**,**o** and **r**. Scale bars: 25 µm (**a**) and 50 µm (**l**). Illustrations in **n** created in BioRender (Lee, J. https://BioRender.com/0bkvepw; 2025).

expression of *Ripk3* (encoding receptor-interacting protein kinase 3) and other necroptosis-related genes in tumour cells (Fig. 3g,h and Supplementary Data 9). Consistent with these findings, the FPR1 signalling transcriptional signature in tumour cells was inversely correlated with a necroptosis gene signature in GBM scRNA-seq data[11,28] (Fig. 3j,i). Furthermore, in FPR1-deficient GL261 cells, which were identified by luciferase expression, we detected increased phosphorylation of the necroptosis executioner pMLKL using immunofluorescence[29] (Fig. 3k–m).

We next used human GBM isolates to examine the effects of FPR1 signalling on tumour-cell necroptosis induced by the pan-caspase inhibitor ZVAD-FMK, the protein-synthesis inhibitor cycloheximide and tumour necrosis facto as described previously[30] (Fig. 3n and Supplementary Table 2). Treatment of three independent GBM isolates with the FPR1 agonist ANXA1 decreased necroptosis, as detected by pMLKL quantification; by contrast, treatment with an FPR1-blocking antibody abrogated the anti-necroptotic effect of ANXA1 (Fig. 3o and Extended Data Fig. 6a b).

To further investigate the role of necroptosis in tumour immunity, we generated two GL261 lines expressing a RIPK3 variant that is activatable by small-molecule-induced dimerization (GL261–RIPK3^{act})[31] (Fig. 3p and Extended Data Fig. 6c,d). We implanted mice with a mix of 70% wild-type GL261 and 30% GL261–RIPK3^{act} cells and intravenously administered the brain-penetrant inducer of RIPK3 dimerization 5 days later (Fig. 3p). The induction of necroptosis in a fraction of glioma cells resulted in a significant extension of survival (Fig. 3q).

As well as promoting cell death, necroptosis activates NF-κB and other pathways that boost the expression of pro-inflammatory molecules and may support antitumour immunity[18]. Indeed, activation of necroptosis in vivo increased the abundance of tumour-infiltrating conventional dendritic cell 1 (cDC1), whereas cDC2s were decreased (Extended Data Fig. 6e,f). Furthermore, GL261-associated antigen GARC-1-specific[32] and IFNγ-producing CD8$^+$ T cells were increased when necroptosis was induced (Fig. 3r and Extended Data Fig. 6g). Conversely, tumour-infiltrating T cells displayed decreased expression of IL-10, TIM3 and FOXP3 in mice bearing necroptosis-activated GL261-RIPK3^{act} tumours (Extended Data Fig. 6h–k).

In complementary in vitro experiments, we generated a GL261 line co-expressing RIPK3^{act} and the model antigen OVA (GL261–RIPK3^{act}/OVA; Extended Data Fig. 6d). We then generated tumour-cell lysates from GL261–RIPK3^{act}/OVA cells treated with the inducer of RIPK3 dimerization to induce necroptosis or vehicle (Extended Data Fig. 6l). Mouse splenic dendritic cells (DCs) treated with lysate from necroptotic GL261–RIPK3^{act}/OVA cells had an increased ability to activate OT-1 T cell receptor-transgenic OVA-specific CD8$^+$ T cells (Extended Data Fig. 6m–w). Together, these findings indicate that disruption of ANXA1-driven FPR1 signalling unleashes GBM cell necroptosis, which boosts glioma-specific immunity.

ANXA1 limits astrocyte inflammatory response

ANXA1 is localized in the membrane, cytoplasm or nucleus and modulates biological responses in the cells that express it[33]; we also detected ANXA1 secretion by astrocytes (Extended Data Fig. 7a). Thus, we investigated the effect of FPR1–ANXA1 interactions on astrocyte responses. First, we analysed the effect of *Fpr1* inactivation in GL261 cells implanted intracranially into wild-type B6 mice. In RNA-seq analyses, astrocytes from mice implanted with *Fpr1*-inactivated GL261 cells displayed increased pro-inflammatory signalling, including NF-κB and NLRP3 inflammasome pathways, compared with astrocytes from control GL261-implanted mice (Fig. 4a–c and Supplementary Data 10). Indeed, in immunofluorescence validation studies, we detected increased ASC speck formation and nuclear NF-κB (indicative of activation) in TME astrocytes after *Fpr1* inactivation in GL261 cells (Fig. 4d–f).

To establish the role of ANXA1 in the regulation of inflammasome and NF-κB activation in human cells, we co-cultured human astrocytes with GBM cells and quantified inflammasome and NF-κB activation following stimulation with lipopolysaccharide (LPS) followed by polyinosinic:polycytidylic acid (poly(I:C)) as described previously[34] (Fig. 4g). We found that LPS and poly(I:C) treatment induced ASC speck formation and IL-1β cleavage (Fig. 4h–j and Extended Data Fig. 7b). Similarly, treatment with TNF and IL-1β induced NF-κB nuclear localization (Fig. 4k and Extended Data Fig. 7c). However, co-culture with GBM cells abrogated these responses (Fig. 4h–k and Extended Data Fig. 7b,c). Moreover, the FPR1 inhibitor T-0080, which blocks the FPR1 interaction site with ANXA1 (ref. 35), or an anti-FPR1 blocking antibody rescued the pro-inflammatory responses of co-cultured astrocytes (Fig. 4i–k).

To complement these findings, we evaluated the effect of *Anxa1* inactivation in astrocytes in the GL261 orthotopic model in B6 wild-type mice. To inactivate *Anxa1* in astrocytes, we injected the retro-orbital sinus of wild-type B6 mice with 5×10^{12} genome copies of PHP.eB serotype adeno-associated virus (AAV-PHP.eB) encoding sg*Anxa1* or sg*Rosa26* under the U6 promoter and *Staphylococcus aureus Cas9* (Sa*Cas9*) under the *GFAP* promoter GfaABC$_1$D expressed in astrocytes (Fig. 4l and Extended Data Fig. 7d,e). Three weeks later, GL261 cells were implanted by intracranial injection. *Anxa1* inactivation in astrocytes extended survival (Fig. 4m). We validated this beneficial effect in independent studies in which we used a lentivirus-based CRISPR–Cas9 system to knockdown *Anxa1* in astrocytes (Extended Data Fig. 7f,g). The extension of survival resulting from *Anxa1* inactivation in astrocytes was concomitant with the upregulation of pro-inflammatory astrocyte responses, as determined by the increased expression detected by RNA-seq of transcriptional modules associated with IL-1 and NF-κB signalling in astrocytes (Extended Data Fig. 7h,i and Supplementary Data 11). *Anxa1* inactivation in astrocytes also resulted in decreased glioma cell G-protein-coupled receptor (GPCR) signalling, which is consistent with the mechanism of ANXA1-induced FPR1 signalling because FPRs are GPCRs[36] (Extended Data Fig. 7j). Moreover, *Anxa1* inactivation in astrocytes also led to increased ASC speck formation, as determined by immunofluorescence (Fig. 4n and Extended Data Fig. 7k), which is concomitant with increased pMLKL expression in tumour cells (Fig. 4o). However, astrocyte-specific *Anxa1* inactivation provided only a minor survival benefit in immunodeficient *Rag2*$^{-/-}$ mice (Extended Data Fig. 7l), supporting a role for astrocyte-produced ANXA1 in the suppression of the adaptive immune response to the tumour. Taken together, these findings indicate that ANXA1 suppresses astrocyte pro-inflammatory responses driven by NF-κB and the inflammasome in astrocytes, and it also limits glioma-cell necroptosis and antitumour immunity.

ANXA1–FPR1 disruption boosts GBM immunity

Astrocytes control myeloid and T cell responses in the central nervous system (CNS)[37–41]. ANXA1 is reported to promote immunosuppression[33], indicating that ANXA1-expressing astrocytes could limit tumour-specific T cells. We therefore analysed the T cell response to glioma after the inactivation of *Fpr1* in GL261 cells or *Anxa1* in astrocytes (Extended Data Fig. 8a). Tumour-infiltrating CD8$^+$ T cells displayed increased expression of numerous pathways associated with T cell receptor signalling, such as NUR77 and CD28, and co-stimulatory pathways, such as ICOS, OX40 signalling and cytotoxicity in recipients of *Fpr1*-deficient GL261 cells (Fig. 5a,b and Supplementary Data 12). Similarly, in CD4$^+$ T cells we detected increased expression of transcriptional modules linked to T cell activation, proliferation, survival, T helper 1 (T_H1) cell polarization and memory formation (Fig. 5c,d and Supplementary Data 13). Furthermore, *Fpr1* inactivation in GL261 cells also triggered the activation of transcriptional programs linked to antitumour responses in TAMs derived from monocytes and microglia, such as those linked to antigen presentation, phagocytosis and pro-inflammatory cytokine signalling (Extended Data Fig. 8b,c and Supplementary Data 14 and 15).

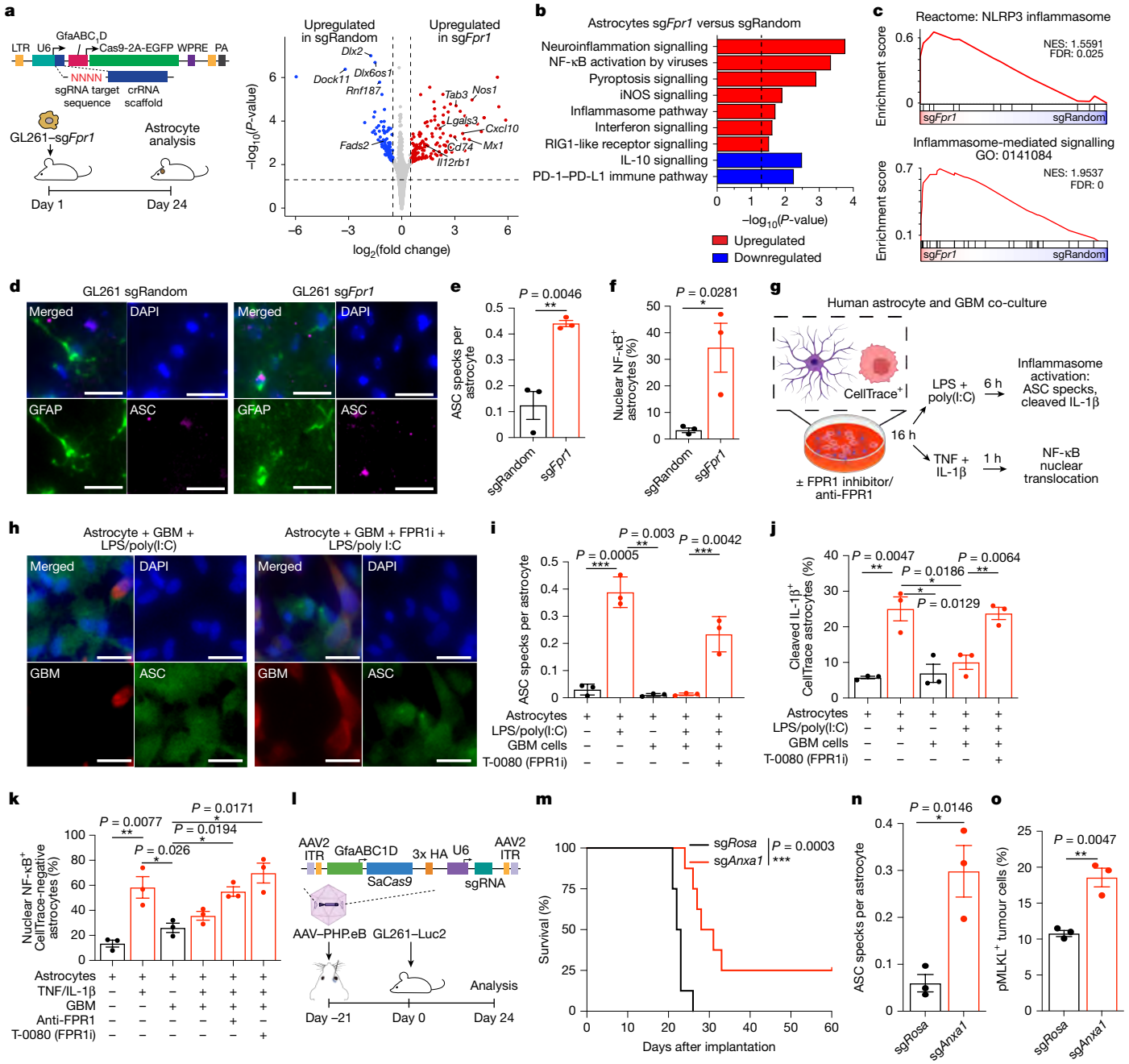

Fig. 4 | ANXA1 inhibits astrocyte immune responses. a–**c**, RNA-seq of astrocytes from GL261 sg*Fpr1* or sgRandom-bearing mice. Volcano plot (**a**) and pathway analysis (**b**,**c**) are shown ($n = 3$ sg*Fpr1* and $n = 4$ sgRandom mice). **d**–**f**, Immunofluorescence of ASC (**d**,**e**) and nuclear NF-κB (**f**) in peritumoral GFAP-positive luciferase-negative astrocytes. Each point represents one mouse ($n = 3$ mice per group). **g**–**j**, Co-culture of primary human astrocytes with CellTrace-labelled primary GBM cultures in the presence or absence of LPS and poly(I:C) ± FPR1 inhibitor (FPR1i) T-0080 (**g**, top right arm), followed by immunofluorescence staining for ASC (**h**,**i**) or cleaved IL-1β (**j**) ($n = 3$ replicate wells per group). **k**, Co-culture of primary human astrocytes with CellTrace-labelled primary GBM cultures in the presence or absence of TNF and IL-1β, FPR1 inhibitor T-0080 and neutralizing anti-FPR1 antibody (**g**, schematic, bottom right arm), staining for nuclear NF-κB. **l**,**m**, AAV construct and GBM mouse model timeline for survival, RNA-seq and immunofluorescence analysis (**l**). Kaplan–Meier survival plot of GL261-bearing mice, transduced with sg*Rosa* or sg*Anxa1* AAV-PHP.eB under the *GFAP* promoter (**m**); $n = 8$ mice per group, log rank. **n**, Immunofluorescence staining of ASC, GFAP and DAPI in peritumoral regions from GL261-bearing mice from day 24. Each point represents one mouse; $n = 3$ mice per group. **o**, Immunofluorescence staining of pMLKL and DAPI in tumour-cell regions from mice that underwent genetic inactivation of *Anxa1*, followed by implantation of GL261. Each point represents a different mouse; $n = 3$ mice per group. In **e**,**f**,**i**,**j**,**k**,**m**,**n** and **o**, there was one replicate experiment, which was performed three times with similar results. $^{***}P < 0.001$, $^{**}P < 0.005$, $^{*}P < 0.05$. *P* values were from unpaired two-tailed *t*-tests (**e**,**f**,**i**,**j**,**k**,**n** and **o**). Data are mean ± s.e.m. (**e**,**f**,**i**,**j**,**k**,**n** and **o**). Scale bars, 25 µm. Illustrations in **g** created in BioRender (Lee, J. https://BioRender.com/0bkvepw; 2025).

In support of these findings, in flow-cytometry studies, *Fpr1* inactivation in GL261 cells was linked to an increase in tumour-infiltrating $CD8^+$ T cells reactive with the GL261-associated antigen GARC-1 (ref. 32) (Fig. 5e) and decreased expression of the exhaustion markers PD-1 and TIM-3, as well as the terminal exhaustion phenotype $PD\text{-}1^+TIM\text{-}3^+SLAMF6^-$ (ref. 42) (Fig. 5f,g). We also detected a decrease in $FOXP3^+$ regulatory T cells, $IL\text{-}10^+$ and $IL\text{-}10^+FOXP3^-$ $CD4^+$ T cells, and an increase in $IL\text{-}2^+$ $CD4^+$ T cells (Extended Data Fig. 9a–d). Conversely,

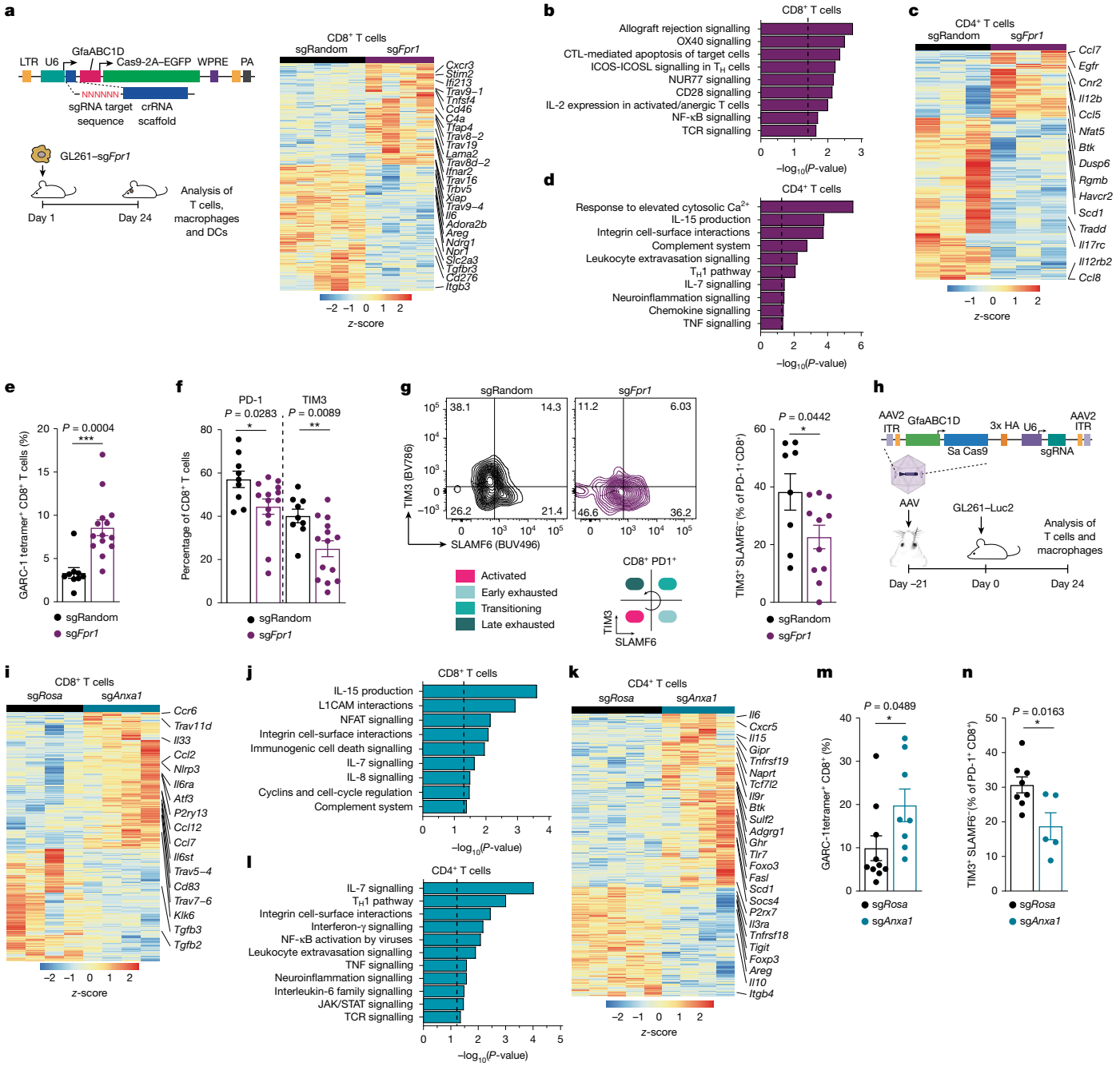

Fig. 5 | Disruption of astrocyte–glioma ANXA1–FPR1 crosstalk enhances anti-tumour immunity. a–**d**, Experimental schematic and bulk RNA-seq analysis of CD8$^+$ (**a**,**b**) and CD4$^+$ (**c**,**d**) T cells from GL261 sg*Fpr1*-implanted mice. DEGs (**a**,**c**) and pathway analysis (**b**,**d**) are shown; $n = 3$ mice per *sgFpr1* group and $n = 5$ mice for the *sgRandom* group. **e**–**g**, Flow-cytometry analysis of CD8$^+$ T cells from GL261 sg*Fpr1*-bearing mice. CD8$^+$ T cells stained for tumour-specific antigen GARC-1 (**e**; $n = 9$ for sg*Rosa26* and $n = 14$ for sg*Fpr1*; two-sided unpaired *t*-test) or exhaustion markers (**f**, PD-1; **g**, TIM3) are shown ($n = 9$ mice for GL261 sgRandom and $n = 14$ mice for GL261 sg*Fpr1*; two-sided unpaired *t*-test). **h**–**l**, Schematic (**h**) and bulk RNA-seq analysis of CD8$^+$ (**i**,**j**) and CD4$^+$ (**k**,**l**) T cells sorted from GL261-implanted mice after AAV-mediated genetic *Anxa1* inactivation in astrocytes ($n = 4$ mice for sg*Anxa1*, CD8$^+$ and CD4$^+$; $n = 4$ mice for CD8$^+$; $n = 5$ mice for CD4$^+$ T cell sg*Rosa* group). DEGs (**i**,**k**) and pathway analysis (**j**,**l**) are shown. **m**,**n**, Flow-cytometry analysis of CD8$^+$ T cells from GL261-bearing mice after genetic *Anxa1* inactivation in astrocytes. CD8$^+$ T cells were stained with tetramers loaded with the tumour-specific antigen GARC-1 (**m**; $n = 10$ for sg*Rosa26* and $n = 8$ for sg*Anxa1*; two-sided unpaired *t*-test), SLAMF6 and exhaustion markers PD-1 and TIM-3 ($n = 8$ for sg*Rosa* and $n = 5$ for sg*Anxa1*; two-sided unpaired *t*-test). Data in **e**,**f**,**g**,**m** and **n** represent pooled data from three separate experiments. ***$P < 0.0005$, **$P < 0.01$, *$P < 0.05$. Data are mean ± s.e.m. (**e**,**f**,**g**,**m** and **n**).

Fpr1 overexpression in GL261 cells resulted in decreased GARC1-specific CD8$^+$ T cells and CD8$^+$ T cells undergoing degranulation; it also reduced IFNγ and TNF production (Extended Data Fig. 9e–h).

These changes in T cells in the TME of mice implanted with *Fpr1*-deficient GL261 cells were concomitant with increased cDC1s and monocytic DCs, decreased cDC2s, upregulation of pro-inflammatory pathways and downregulation of anti-inflammatory signalling (Extended Data Fig. 9i–n and Supplementary Data 16–18). These findings are of particular importance in light of the role of cDC1 in promoting tumour immunity[43,44]. Thus, FPR1 regulates GBM necroptosis and limits immunogenic signalling in DCs and T cell activation.

Further support for a role of ANXA1–FPR1 signalling in the control of glioma immunity was provided by analysis of the effects of *Anxa1* inactivation in astrocytes, which resulted in the upregulation of transcriptional modules linked to T cell receptor signalling, proliferation, trafficking, cytotoxicity and memory differentiation in tumour-infiltrating $CD8^+$ T cells, as determined by RNA-seq (Fig. 5h–j and Supplementary Data 19). *Anxa1* inactivation in astrocytes also led to increased expression of genes linked to T_H1 cell differentiation, IFNγ, TNF and IL-7 signalling in $CD4^+$ T cells (Fig. 5k,l and Supplementary Data 20). In agreement with these findings, FACS analyses of tumour-infiltrating $CD8^+$ T cells detected an increase in GARC-1-reactive $CD8^+$ T cells following *Anxa1* inactivation in astrocytes (Fig. 5m), concomitant with reduced expression of the exhaustion markers PD-1 and TIM-3 and a decrease in $CD8^+$ T cells displaying the terminally exhausted T cell phenotype $PD\text{-}1^+TIM\text{-}3^+SLAMF6^-$ (Fig. 5n and Extended Data Fig. 9o,p). Furthermore, *Anxa1* inactivation in astrocytes led to the activation of numerous transcriptional programs linked to activation and antitumour TAM responses (Extended Data Fig. 9q,r and Supplementary Data 21 and 22). These findings indicate that FPR1–ANXA1 glioma–astrocyte interactions limit tumour-specific T cell responses.

Discussion

The immunosuppressive nature of the TME represents a substantial challenge for the success of immunotherapy in GBM. It is therefore important to define TME mechanisms that limit the immune response to GBM. Indeed, immunosuppressive mechanisms driven by TAMs[5,8] and neutrophils[45] have been described in the GBM TME. However, despite their roles in the immune response to infection, neurodegeneration, autoimmunity and brain metastases[9,46], astrocytes are under-studied in GBM. For example, astrocytes secrete immunosuppressive cytokines when co-cultured with GBM tumour cells[47], but the study of astrocytes in bulk precluded the identification of the specific astrocyte subsets and mechanisms involved. Using RABID-seq to study of TME cell–cell communication with single-cell resolution, we established that bidirectional astrocyte–GBM interactions mediated by ANXA1 and FPR1 promote tumour immunoevasion.

ANXA1 is a calcium-dependent phospholipid-binding protein that regulates cellular responses in the cells that express it and also in neighbouring cells expressing FPR[33]. ANXA1 expression and secretion are induced by glucocorticoids[48], which are prescribed to nearly all patients with GBM at some point in their disease course. ANXA1 contributes to the immune-suppressive activities of glucocorticoids through multiple mechanisms, including the inhibition of cytosolic phospholipase A_2 (PLA_2)[48] and inducible nitric oxide synthetase (iNOS)[49], and also through the induction of anti-inflammatory cytokines such as IL-10 (ref. 50). ANXA1 has also been reported to inhibit NLRP3 inflammasome activation in macrophages, suppressing the production of active IL-1β[51]. We have shown that cytosolic PLA_2 promotes NF-κB activation in astrocytes[52], driving pro-inflammatory responses characterized by the expression of iNOS, IL-1β and other molecules that promote CNS inflammation, and also activating microglia and other cell types. Thus, ANXA1 inhibits pathways that drive immunostimulatory responses in astrocytes and other cells in the GBM TME.

FPR signalling is reported to boost the invasiveness and proliferative capacity of GBM cells[53], but its effects on tumour-specific immunity have remained unknown. Here we show that FPR1 signalling inhibits necroptosis in GBM cells and tumour-specific immunity. Indeed, necroptosis has been shown to promote tumour-specific immune responses through the release of tumour-associated antigens in combination with pro-inflammatory signals[18,54]. However, the role of necroptosis in GBM has thus far been unclear[55]. RIPK1 and RIPK3 activation during necroptosis increases cytosolic calcium levels[56]. A similar increase occurs following FPR1 blockade[35], and increased cytosolic calcium levels lower the threshold for necroptosis[57]. As a result, FPR1 signalling is likely to suppress tumour-cell necroptosis by decreasing intracellular calcium levels. These effects of FPR1 signalling might also modulate calcium-dependent bidirectional GBM-neuron interactions that promote tumour progression[58]. Although ANXA1–FPR1 signalling may have context- and cell type-dependent effects[35], our study links astrocyte–glioma communication through ANXA1–FPR1 to the modulation of the immune response to GBM.

In summary, we have developed a barcoding approach to analyse TME cell–cell interactions with single-cell resolution in clinical samples and preclinical models. This innovative approach could be extended to other CNS and peripheral diseases, provided that the tissue-processing methods used prevent the exclusion of specific cell types of interest[3,17]. Our barcoding approach identified ANXA1–FPR1 astrocyte–GBM communication as a promoter of immunoevasion and tumour progression. Future studies should combine the barcoding of TME cell interactions with spatial analyses[16], to further define the role of astrocytes in TME niches linked to GBM recurrence[16]. Nevertheless, our findings support targeting of ANXA1–FPR1 signalling with CNS-penetrant inhibitors[35] or other modalities to boost the efficacy of GBM immunotherapies such as vaccination[14], CAR T cells[59] or immune checkpoint blockade[60].

Online content

Any methods, additional references, Nature Portfolio reporting summaries, source data, extended data, supplementary information, acknowledgements, peer review information; details of author contributions and competing interests; and statements of data and code availability are available at https://doi.org/10.1038/s41586-025-09191-9.

1. van den Bent, M. J. et al. Primary brain tumours in adults. *Lancet* **402**, 1564–1579 (2023).
2. Andersen, B. M. et al. Glial and myeloid heterogeneity in the brain tumour microenvironment. *Nat. Rev. Cancer* **21**, 786–802 (2021).
3. Clark, I. C. et al. Barcoded viral tracing of single-cell interactions in central nervous system inflammation. *Science* **372**, eabf1230 (2021).
4. Mathewson, N. D. et al. Inhibitory CD161 receptor identified in glioma-infiltrating T cells by single-cell analysis. *Cell* **184**, 1281–1298.e26 (2021).
5. Takenaka, M. C. et al. Control of tumor-associated macrophages and T cells in glioblastoma via AHR and CD39. *Nat. Neurosci.* **22**, 729–740 (2019).
6. Kirschenbaum, D. et al. Time-resolved single-cell transcriptomics defines immune trajectories in glioblastoma. *Cell* **187**, 149–165 (2024).
7. Hara, T. et al. Interactions between cancer cells and immune cells drive transitions to mesenchymal-like states in glioblastoma. *Cancer Cell* **39**, 779–792 (2021).
8. Friebel, E. et al. Single-cell mapping of human brain cancer reveals tumor-specific instruction of tissue-invading leukocytes. *Cell* **181**, 1626–1642 (2020).
9. Lee, H.-G., Wheeler, M. A. & Quintana, F. J. Function and therapeutic value of astrocytes in neurological diseases. *Nat. Rev. Drug Discov.* **21**, 339–358 (2022).
10. Sofroniew, M. V. Astrocyte barriers to neurotoxic inflammation. *Nat. Rev. Neurosci.* **16**, 249–263 (2015).
11. Couturier, C. P. et al. Glioblastoma scRNA-seq shows treatment-induced, immune-dependent increase in mesenchymal cancer cells and structural variants in distal neural stem cells. *Neuro Oncol.* **24**, 1494–1508 (2022).
12. Müller, S. et al. Single-cell sequencing maps gene expression to mutational phylogenies in PDGF- and EGF-driven gliomas. *Mol. Syst. Biol.* **12**, 889 (2016).
13. Gan, H. K., Kaye, A. H. & Luwor, R. B. The EGFRvIII variant in glioblastoma multiforme. *J. Clin. Neurosci.* **16**, 748–754 (2009).
14. Keskin, D. B. et al. Neoantigen vaccine generates intratumoral T cell responses in phase Ib glioblastoma trial. *Nature* **565**, 234–239 (2019).
15. Ravi, V. M. et al. Spatially resolved multi-omics deciphers bidirectional tumor-host interdependence in glioblastoma. *Cancer Cell* **40**, 639–655 (2022).
16. Greenwald, A. C. et al. Integrative spatial analysis reveals a multi-layered organization of glioblastoma. *Cell* **187**, 2485–2501 (2024).
17. Saunders, A. et al. Ascertaining cells' synaptic connections and RNA expression simultaneously with barcoded rabies virus libraries. *Nat. Commun.* **13**, 6993 (2022).
18. Weinlich, R., Oberst, A., Beere, H. M. & Green, D. R. Necroptosis in development, inflammation and disease. *Nat. Rev. Mol. Cell Biol.* **18**, 127–136 (2017).
19. Callow, M. G. et al. CRISPR whole-genome screening identifies new necroptosis regulators and *RIPK1* alternative splicing. *Cell Death Dis.* **9**, 261 (2018).
20. Levy, A. et al. CD38 deficiency in the tumor microenvironment attenuates glioma progression and modulates features of tumor-associated microglia/macrophages. *Neuro Oncol.* **14**, 1037–1049 (2012).
21. Ma, K., Chen, S., Chen, X., Zhao, X. & Yang, J. CD93 is associated with glioma-related malignant processes and immunosuppressive cell infiltration as an inspiring biomarker of survivance. *J. Mol. Neurosci.* **72**, 2106–2124 (2022).

22. Yang, F., Zhang, X., Wang, X., Xue, Y. & Liu, X. The new oncogene transmembrane protein 60 is a potential therapeutic target in glioma. *Front. Genet.* **13**, 1029270 (2022).
23. Mu, L. et al. Pan-cancer analysis of ASB3 and the potential clinical implications for immune microenvironment of glioblastoma multiforme. *Front. Immunol.* **13**, 842524 (2022).
24. Lu, B. et al. Basic transcription factor 3 like 4 enhances malignant phenotypes through modulating tumor cell function and immune microenvironment in glioma. *Am. J. Pathol.* **194**, 772–784 (2024).
25. Ma, K., Chen, S., Chen, X., Yang, C. & Yang, J. S100A10 is a new prognostic biomarker related to the malignant molecular features and immunosuppression process of adult gliomas. *World Neurosurg.* **165**, e650–e663 (2022).
26. Walther, A., Riehemann, K. & Gerke, V. A novel ligand of the formyl peptide receptor: annexin I regulates neutrophil extravasation by interacting with the FPR. *Mol. Cell* **5**, 831–840 (2000).
27. Puchalski, R. B. et al. An anatomic transcriptional atlas of human glioblastoma. *Science* **360**, 660–663 (2018).
28. Guo, K. et al. A novel necroptosis-related gene signature for predict prognosis of glioma based on single-cell and bulk RNA sequencing. *Front. Mol. Biosci.* **9**, 984712 (2022).
29. Sun, L. et al. Mixed lineage kinase domain-like protein mediates necrosis signaling downstream of RIP3 kinase. *Cell* **148**, 213–227 (2012).
30. Chesnokov, M., Khan, I. & Chefetz, I. Induction and detection of necroptotic cell death in mammalian cell culture. *Methods Mol. Biol.* **2255**, 119–134 (2021).
31. Orozco, S. et al. RIPK1 both positively and negatively regulates RIPK3 oligomerization and necroptosis. *Cell Death Differ.* **21**, 1511–1521 (2014).
32. Iizuka, Y. et al. Identification of a glioma antigen, GARC-1, using cytotoxic T lymphocytes induced by HSV cancer vaccine. *Int. J. Cancer* **118**, 942–949 (2006).
33. Gerke, V. et al. Annexins—a family of proteins with distinctive tastes for cell signaling and membrane dynamics. *Nat. Commun.* **15**, 1574 (2024).
34. Franchi, L. et al. Cytosolic double-stranded RNA activates the NLRP3 inflammasome via MAVS-induced membrane permeabilization and K^+ efflux. *J. Immunol.* **193**, 4214–4222 (2014).
35. Li, Z. et al. Formyl peptide receptor 1 signaling potentiates inflammatory brain injury. *Sci. Transl. Med.* **13**, eabe9890 (2021).
36. Weiß, E. & Kretschmer, D. Formyl-peptide receptors in infection, inflammation, and cancer. *Trends Immunol.* **39**, 815–829 (2018).
37. Sanmarco, L. M. et al. Gut-licensed $IFN\gamma^+$ NK cells drive $LAMP1^+TRAIL^+$ anti-inflammatory astrocytes. *Nature* **590**, 473–479 (2021).
38. Wheeler, M. A. et al. MAFG-driven astrocytes promote CNS inflammation. *Nature* **578**, 593–599 (2020).
39. Wheeler, M. A. et al. Environmental control of astrocyte pathogenic activities in CNS inflammation. *Cell* **176**, 581–596 (2019).
40. Wheeler, M. A. et al. Droplet-based forward genetic screening of astrocyte-microglia cross-talk. *Science* **379**, 1023–1030 (2023).
41. Kiss, M. G. et al. Interleukin-3 coordinates glial-peripheral immune crosstalk to incite multiple sclerosis. *Immunity* **56**, 1502–1514 (2023).
42. Schnell, A. et al. Stem-like intestinal Th17 cells give rise to pathogenic effector T cells during autoimmunity. *Cell* **184**, 6281–6298 (2021).
43. Meiser, P. et al. A distinct stimulatory cDC1 subpopulation amplifies $CD8^+$ T cell responses in tumors for protective anti-cancer immunity. *Cancer Cell* **41**, 1498–1515 (2023).
44. Bowman-Kirigin, J. A. et al. The conventional dendritic cell 1 subset primes $CD8^+$ T cells and traffics tumor antigen to drive antitumor immunity in the brain. *Cancer Immunol. Res.* **11**, 20–37 (2023).
45. Maas, R. R. et al. The local microenvironment drives activation of neutrophils in human brain tumors. *Cell* **186**, 4546–4566.e27 (2023).
46. Priego, N. et al. STAT3 labels a subpopulation of reactive astrocytes required for brain metastasis. *Nat. Med.* **24**, 1024–1035 (2018).
47. Heiland, D. H. et al. Tumor-associated reactive astrocytes aid the evolution of immunosuppressive environment in glioblastoma. *Nat. Commun.* **10**, 2541 (2019).
48. Pepinsky, R. B. et al. Purification and partial sequence analysis of a 37-kDa protein that inhibits phospholipase A2 activity from rat peritoneal exudates. *J. Biol. Chem.* **261**, 4239–4246 (1986).
49. Wu, C. C. et al. Lipocortin 1 mediates the inhibition by dexamethasone of the induction by endotoxin of nitric oxide synthase in the rat. *Proc. Natl Acad. Sci. USA* **92**, 3473–3477 (1995).
50. Ferlazzo, V. et al. Anti-inflammatory effects of annexin-1: stimulation of IL-10 release and inhibition of nitric oxide synthesis. *Int. Immunopharmacol.* **3**, 1363–1369 (2003).
51. Sanches, J. M. et al. Annexin A1 regulates NLRP3 inflammasome activation and modifies lipid release profile in isolated peritoneal macrophages. *Cells* **9**, 926 (2020).
52. Chao, C.-C. et al. Metabolic control of astrocyte pathogenic activity via cPLA2-MAVS. *Cell* **179**, 1483–1498 (2019).
53. Zhou, Y. et al. Formylpeptide receptor FPR and the rapid growth of malignant human gliomas. *J. Natl Cancer Inst.* **97**, 823–835 (2005).
54. Yatim, N. et al. RIPK1 and NF-κB signaling in dying cells determines cross-priming of $CD8^+$ T cells. *Science* **350**, 328–334 (2015).
55. Han, M. et al. Regulated cell death in glioma: promising targets for natural small-molecule compounds. *Front. Oncol.* **14**, 1273841 (2024).
56. Sun, W. et al. Cytosolic calcium mediates RIP1/RIP3 complex-dependent necroptosis through JNK activation and mitochondrial ROS production in human colon cancer cells. *Free Radic. Biol. Med.* **108**, 433–444 (2017).
57. Nomura, M., Ueno, A., Saga, K., Fukuzawa, M. & Kaneda, Y. Accumulation of cytosolic calcium induces necroptotic cell death in human neuroblastoma. *Cancer Res.* **74**, 1056–1066 (2014).
58. Venkataramani, V. et al. Glutamatergic synaptic input to glioma cells drives brain tumour progression. *Nature* **573**, 532–538 (2019).
59. Bagley, S. J. et al. Intrathecal bivalent CAR T cells targeting EGFR and IL13Rα2 in recurrent glioblastoma: phase 1 trial interim results. *Nat. Med.* **30**, 1320–1329 (2024).
60. Lim, M. et al. Phase III trial of chemoradiotherapy with temozolomide plus nivolumab or placebo for newly diagnosed glioblastoma with methylated MGMT promoter. *Neuro Oncol.* **24**, 1935–1949 (2022).

Methods

Human samples and RABID-seq of organotypic GBM cultures

Human GBM fresh tumour tissue specimens were allocated by the Neuropathology Division and the Tissue and Blood Repository at Brigham and Women's Hospital in accordance with prospective consent to a tissue-procurement institutional review board protocol for CNS disorders or institutional review board waiver of consent. Tissue was immediately placed in hibernate A (Gibco, A1247501) medium using an aseptic technique. Fragments of tissue were gently cut into pieces of about 2 mm^3 for cultures on Millicell transwell membranes (EMD Millipore, PICM03050) in neurobasal A medium (Thermo Fisher Scientific, 17504044) supplanted with 1× B27 (Gibco, 12349015). The transwell system contained 1 ml of medium below the membrane, fitted into a 6-well tissue-culture plate, with the slice resting on the membrane, covered with a thin film of medium (roughly 5 µl) for optimal oxygen diffusion. The liquid film was maintained by pipetting 5 µl of medium onto slices from the lower chamber daily. The medium in the lower well was replaced every 48 h. The EF1α promoter was cloned into the pBOB-SynP-HTB plasmid, which contains a lentiviral backbone and was a gift from E. Callaway and L. Luo (Addgene plasmid 30195) . Lentivirus was produced from newly cloned pBOB-EF1α-HTB using previously described methods[38].

On the first day of culture, each piece of tissue was lentivirally transduced with TVA and G under the EF1α promoter, which was pipetted on top of cultures in a volume of 5 µl at a concentration of 10^6 infectious units. One day later, tissue was gently rinsed with PBS, which was removed to leave a thin liquid film on the top of each slice. After 5 days, tissues were injected with 1 µl of barcoded, pseudotyped rabies virus (EnvA-RABΔG) at a concentration of 1,000 infectious units per microlitre. One day later, tissue was gently rinsed with PBS, which was removed to leave a thin liquid film on the top of each slice. After 5 days, tissue was digested using papain, followed by trituration using fire-polished glass Pasteur pipettes. Cells then underwent myelin removal using a myelin removal kit (Miltenyi Biotec, 130-096-733). Filtered cell suspensions then underwent fluorescence-activated cell sorting (FACS) for $mCherry^+$ cells. Sorted $mCherry^+$ cells then underwent single-cell droplet encapsulation using Indrop v3 switch drops, followed by cDNA library preparation at the Single Cell Core at Harvard Medical School. Before sequencing, mCherry barcodes were amplified using 3′ cDNA primers and a primer to mCherry as described previously[3].

Mice

Inbred C57BL/6J mice (Jackson Laboratory, 000664) were used as a genetic background for in vivo experiments. Mice were housed under standard conditions in a pathogen-free facility at the Hale Building for Transformative Medicine at 20–23 °C and 50% humidity with access to water and food ad libitum and under a 12 h:12 h light:dark cycle, in accordance with guidelines defined by the Institutional Animal Care and Use Committee (IACUC).

Cell culture

GL261-Luc2 cells (Caliper Life Sciences) were cultured in high-glucose DMEM (Gibco, 11965118) supplemented with 10% fetal bovine serum (FBS; Gibco, 10-438-026), 1% penicillin/streptomycin (Thermo Fisher Scientific, 15140122) and 100 µg ml^{-1} G418 Geneticin (Thermo Fisher Scientific, 10131027). Patient-derived human GBM lines BT485, BT482 and BT1018 were generated with prospective patient consent and obtained through the Dana-Farber Cancer Institute Center for Patient Derived Models (available at models@dfci.harvard.edu). These lines were kept in NeuroCult NS-A Proliferation Kit Human (StemCell Technologies, 05751) supplemented with B27, N2 (Gibco, 17502-048), 1% penicillin/streptomycin, 1:100 0.2% heparin (StemCell Technologies, 07980), 10 ng ml^{-1} recombinant FGF (Invitrogen, PHG0021) and 20 ng ml^{-1} EGF (PeproTech, AF-100-15). Human astrocytes (ScienCell, 1800) were cultured in high-glucose DMEM containing 10% FBS and expanded at confluency. All cell lines were tested for mycoplasma and authenticated by RNA-seq, short tandem repeat analysis, histological analysis, and pathogen PCR testing by their suppliers.

Generation of GL261 cell lines

For the production of TVA and G-expressing GL261-luc2 cells, the human *GFAP* promoter was cloned into the pBOB-SynP-HTB plasmid, which was a gift from E. Callaway and L. Luo (Addgene plasmid 30195). GL261-Luc2 cells were stably transfected with newly cloned pBOB-GFAP-HTB. GL261 sgRandom, sg*Fpr1* and sg*Fpr2* were generated using the plasmid pLenti- U6-sgScramble-Gfap-Cas9-2A-EGFP-WPRE lentiviral backbone, as described previously[38]. This backbone contains derivatives of the previously described reagents lentiCRISPR v2 (a gift from F. Zhang; Addgene plasmid 2961) and lentiCas9-EGFP (a gift from P. Sharp and F. Zhang; Addgene plasmid 63592). The *Gfap* promoter is the ABC_1D *gfa2 GFAP* promoter[61]. PCR-based restriction cloning was done to exchange sgRNA sequences 20 nucleotides long to target different genes using Phusion HF Master Mix (Thermo Fisher Scientific, F-548S) and the following primers: U6-PCR-F, 5′-AAAGGCGCGCCGAGGGCCTATTT-3′; U6-PCR-R, 5′-TTTTTTGGTCTCCCGGTGTTTCGTCCTTTCCAC-3′; cr-RNA-R, 5′-GTTCCCTGCAGGAAAAAAGCACCGA-3′; and cr-RNA-F, 5′-AAAAAAGGTCTCTACCG$(N)_{20}$GTTTTAGAGCTAGAAATAGCAAGTT-3′, where N_{20} marks the sgRNA substitution site. The sgRNAs were designed using a combination of tools: Synthego (https://design.synthego.com/#/); CRISPick (SpyoCas9, Hsu (2013) tracrRNA, https://portals.broadinstitute.org/gppx/crispick/public); and the Sabatini/Lander list (Addgene, 1000000096). The exon-targeting guides that were represented on most sgRNA design platforms and were most upstream were selected. The sgRNA sequences used are as follows: non-targeting random sgRNA. 5′-GCACTACCAGAGCTAACTCA-3′; sg*Fpr1*, 5′-ATTGCCAGCATGGTCATGGG-3′; and sg*Fpr2*, 5′-GCAAACAGCAACAATTGACA-3′.

To generate new GL261 subclonal lines, Lipofectamine 3000 (Thermo Fisher Scientific, L3000008) was used. In brief, 1.5×10^5 cells seeded in 6-well plates were transfected by dropwise addition of DNA–lipid complexes composed of 2.5 µg DNA and 7.5 µl Lipofectamine 3000 in Opti-MEM reduced serum medium + GlutaMAX (Thermo Fisher Scientific, 51985034). Then, 48 h after transfection, antibiotic selection was initiated with 800 µg ml^{-1} zeocin (Invivogen, ant-zn-1) for 2 weeks. Successfully transfected antibiotic-resistant clones were further expanded and maintained at 200 µg ml^{-1} Zeocin thereafter. Gene inactivation in subclonal lines bearing gRNA was confirmed by quantitative PCR. For generation of GL261-RIPK3^{act} and GL261-OVA-RIPK3^{act}, GL261-luc and GL261-OVA lines underwent transfection using Lipofectamine 3000 as described above, using the AO358-pBABE-FLAG-mRIPK3-2xFV-2A-GFP-puro plasmid provided by A. Oberst[31]. Then 48 h after transfection, antibiotic selection was initiated with 2 µg ml^{-1} puromycin (Sigma-Aldrich, P9620-10ML). Construct expression was confirmed by GFP detection and separately by confirmation of cell death after adding B/B homodimerizer (also known as AP-1 or AP20187; Clontech Labs, 635058) as originally described[31]. Successfully transfected, antibiotic-resistant clones were further expanded and maintained at 1 µg ml^{-1} puromycin thereafter. For generation of GL261-FPR1OE, GL261 sgRandom cells underwent transfection using Lipofectamine 3000 using the conditions described above, with the plasmid pUNO-mFPR1 (InVivoGen, puno1-mfpr1). Then, 48 h after transfection, antibiotic selection was initiated using 8 µg ml^{-1} blasticidin (Thermo Fisher Scientific, A1113903). Successfully transfected, antibiotic-resistant clones were further expanded and maintained at 4 µg ml^{-1} blasticidin thereafter. FPR1 overexpression was confirmed by qPCR.

RNA extraction and qPCR

For quantitative analysis of gene transcription from cultured cells, cellular RNA was extracted using the RNeasy Kit (Qiagen, 74004). In brief, cells were lysed in 350 µl RLT buffer and stored at −80 °C until

extraction. RNA was transcribed to cDNA using the High-Capacity cDNA Reverse Transcription Kit (Life Technologies, 4368813). Quantitative measurement of gene expression was performed by qPCR using Taqman Fast Universal PCR Master Mix (Life Technologies, 4367846), MicroAmp Optical 384 well plates (Thermo Fisher Scientific, 43-098-49) and a ViiA 7 Real-Time PCR System (Applied Biosciences). Taqman probes used in this study were *Gapdh* (Mm99999915_g1) and *Fpr1* (Mm00442803_s1). qPCR data were analysed by the $\Delta\Delta C_t$ method by normalizing the expression of each gene for each replicate by the average of the housekeeping gene (*Gapdh*) and then normalizing the treatment group to the control group to determine a relative change.

Orthotopic tumour model and intratumoral delivery

The syngeneic model of glioblastoma was established by intracranial implantation of 1×10^5 GL261-Luc2 cells in 3 µl PBS. In brief, cells were detached using Accutase (Stemcell Technologies, 07920) and cell suspensions prepared in serum-free DMEM. The surgical procedure was done following IACUC guidelines for survival surgery. A small-animal stereotaxic frame (David Kopf Instruments) was positioned within a laminar flow cabinet and a sterile field containing all the surgical instruments and tools was established. The surgical site was shaved and sterilized using isopropyl swabs (Becton Dickinson) and Betadine (Purdue Products). For intracranial injection, mice were placed on the stereotaxic frame and covered with a sterile drape to maintain the sterile field. A 1-cm incision was made on the scalp and the coordinate system was centred on bregma. A hole was drilled at the +1.8 mm (lateral) and +0.5 mm (anterior) position. A 25 µl glass syringe (Hamilton) was inserted to a final depth of 3 mm, and 3 µl of cell suspension was injected at a rate of 1 µl min^{-1}. After a minute, the needle was slowly retracted to avoid liquid backflow. Tumour implantation was confirmed by in vivo bioluminescence imaging. In brief, mice anaesthetized using isoflurane as described above were injected intraperitoneally with 0.15 mg per kg D-luciferin (Cayman Chemical, 14681) in PBS. After 10 min, luminescence was captured at 560 nm wavelength multiple times at high sensitivity and 30 s exposure time using the In-Vivo Xtreme Optical/X-ray imaging system (Bruker). Bruker MI SE v7 (Bruker) software was used to quantify photons per second net of background signal within the area of the mouse skull. Regions of interest were overlaid onto X-ray images to visualize the tumour burden. For GL261-RIPK3^{act} necroptosis induction, B/B homodimerizer or vehicle control was injected retro-orbitally in mice at 5 mg per kg 5 days after tumour implantation.

RABID-seq analysis of GL261

C57BL/6J mice were implanted intracranially with 100,000 GL261-TVA/G cells into the right striatum. Then, 7 or 14 days after implantation, the tumour site was injected with 1 µl EnvA-RABΔG at a concentration of 1,000 infectious units per µl. Seven days after EnvA-RABΔG injection, mice were euthanized and the CNS was isolated using methods identical to those of the human GBM samples above, except that sorted mCherry$^+$ cells underwent single-cell droplet encapsulation using 3′ feature barcode kits from 10X Genomics (1000262).

Design of adeno-associated virus constructs

The sgRNA expression plasmid was derived from pAAV-FLEX-SaCas9-U6-sgRNA (a gift from L. Zweifel (Addgene plasmid 124844), in which the FLEX cassette was removed by PCR and the *GFAP* promoter (ABC_1D *gfa2*) was inserted. Guide RNAs were cloned into the above AAV expression plasmid using annealed oligo cloning as described previously[62]. The most-upstream exon-targeting guide RNA for *Anxa1* was identified using the search function of CRISPick (SpyoCas9, Hsu (2013) tracrRNA, https://portals.broadinstitute.org/gppx/crispick/public): sg*Anxa1*, 5′-GCAAACAGCAACAATTGACA-3′. The sg*Rosa26* was previously published: 5′-GCAAACAGCAACAATTGACA-3′ (ref. 6). The sgRNA cloning was validated by Sanger sequencing (Azenta Life Science) of multiple clones using forward and reverse primers (PCR-F, 5′-CTGAACGGCCTGTACGACGACAAGGACAA-3′, reverse, 5′-GCGCAGAGAGGGAGTGGCCAACTC-3′).

AAV packaging

AAV-PHP.eB was produced with the above sgRNA-expressing plasmids by transfection of HEK293 AAV ProT Cells (Takara, 632273) using polyethylenamine (Polysciences, 23966-1). The pUCmini-iCAP-PHP.eB was a gift from V. Gradinaru (Addgene plasmid 103005) and pAdF6 (Addgene, 112867) was a gift from the lab of J. M. Wilson), as described previously[63]. The AAV was titred by qPCR (Abm, G931) and 5×10^{12} genome copies in 100 µl PBS was administered by a single retro-orbital injection three weeks before tumour implantation.

Isolation of mouse CNS cells

Cells were isolated from mouse brain tissue by intracardiac perfusion of anesthetized mice with 20 ml cold PBS. The brain was dissected, minced and enzymatically dissociated for 20 min at 37 °C and 100 rpm shaking in a solution containing 0.66 mg ml^{-1} papain (Sigma-Aldrich, P4762) in HBSS without Mg/Ca (Thermo Fisher Scientific, 14175095), followed by incubation at the same conditions after the addition of an equal volume of DMEM supplemented with Collagenase D (Roche, 11088858001) and DNase I (Thermo Fisher Scientific, 90083) at 0.66 mg ml^{-1} and 8 U ml^{-1}, respectively. The suspension was dissociated by pipetting and filtered through a 70-µm cell strainer (Thermo Fisher Scientific, 22363548). After centrifugation at 600*g* for 5 min, the pellet was resuspended in 10 ml 30% Percoll (GE Healthcare Biosciences, GE17-0891-01) in PBS and gradient centrifuged at 600*g* for 25 min at the lowest acceleration and deceleration settings. The myelin layer accumulating at the top of the solution was aspirated and the cell pellet was washed with PBS once.

GL261 migration assay

GL261 cells were cultured on transwell membranes (Celltreat, 230633). The chemotactic stimulant was NIH-3T3 (ATCC, CRL-1658) conditioned medium in the bottom, with serum-free medium in the top well, as previously described[64].

Co-culture assays with human astrocytes and GBM cells

For in vitro experiments of astrocyte inflammasome and NF-kB activation, human astrocytes (ScienceCell, 1800) were plated on poly-D-lysine (Thermo Fisher Scientific, A3890401)-coated 96-well plates at 10,000 cells per well. Two days later, primary human GBM cultures (BT1018, BT145 and BT482) were labelled with CellTrace Far Red (Invitrogen, C34564) and added to astrocytes at 10,000 cells per well. The FPR1 inhibitor T-0080 (10 µM, Sigma Adrich, SML3283) or the neutralizing FPR1 antibody (R&D Systems, clone 350418, MAB3744, 4 µg ml^{-1}) were immediately added to the appropriate wells; an equal volume of DMSO, used as the solvent for T-0080, was added to control wells. Co-cultures were left to rest for 2 h before adding 10 ng ml^{-1} LPS (InVivogen, tlrl-eklps) for 3 h followed by 500 ng ml^{-1} high-molecular-weight poly(I:C) (InVivogen, tlrl-pic) for 3 h; or, in experiments measuring nuclear NF-κB, cells were stimulated for 1 h with TNF (R&D Systems, 210-TA, 10 ng ml^{-1}) and IL-1β (R&D Systems, 201-LB, 20 ng ml^{-1}). Cells were then fixed and stained for immunofluorescence microscopy as described below. For in vitro GBM cell necroptosis assays, BT1018, BT145 or BT482 was seeded in 96-well plates at 20,000 cells per well. After two days, recombinant human ANXA1 (R&D Systems, 3770-AN-050, 4 µg ml^{-1}) or the neutralizing FPR1 antibody (R&D Systems, clone 350418, MAB3744, 4 µg ml^{-1}) was added. One hour later, cells were treated with Z-VAD(OMe)-FMK (MedChem Express, HY-16658, 20 µM), cycloheximide (Sigma-Aldrich, 239763-M, 20 µM), followed one hour later by recombinant human TNF (R&D Systems, 210-TA, 20 ng ml^{-1}). An equivalent volume of DMSO was added to control wells. After 8 h, cells were fixed for immunofluorescence microscopy.

Co-culture of GL261-OVA-RIPK3^{act} lysate-pulsed DCs and OT1 CD8 + T cells

GL261-OVA-RIPK3^{act} cells were treated with 0.5% ethanol (Sigma-Aldrich, E7023) or 50 µM B/B homodimerizer for 4 h, and cell cultures/supernatants were collected and washed with PBS then flash-frozen on dry ice, alternating with thawing in a warm water bath five times. Protein concentration was determined by Pierce BCA assay (Thermo Fisher Scientific, 23235). Splenic DCs were isolated from naive mouse spleen using CD11c microbeads (Miltenyi Biotec, 130-125-835) and plated at 5,000 cells per well in a 96-well plate. After 30 min, 10 µg lysate per well and 25,000 per well CellTrace Far Red-labelled OT1 CD8$^+$ T cells (purified using a CD8$^+$ T cell isolation kit; Miltenyi Biotec, 130-096-543) were added. After 72 h, cells were collected for flow cytometry or pulsed with Thymidine for 12 h for scintillation counting.

Immunofluorescence microscopy

Antibodies used for immunofluorescence microscopy were: ASC (Adipogen, AL177; 1:100); cleaved IL-1β (Thermo Fisher Scientific, PA5-105048; 1:200), and NF-κB (Cell Signaling Technology, clone D14E12; 1:100); pMLKL (Abcam, human, ab187091; mouse, ab196436; 1:100); GFAP (Abcam, ab4674; 1:500); Luciferase (BioRad, MCA2076; 1:100); and DAPI (Sigma Aldrich, D9542; 1:1,000). Secondary antibodies were used at 1:1,000 and were: donkey anti-rabbit Alexa Fluor 647 (Invitrogen, A31573); donkey anti-chicken Alexa Fluor 594 (Invitrogen, A21203); goat anti-chicken Alexa Fluor 488 (Invitrogen, A78948); and donkey anti-rabbit Alexa Fluor 488 (Invitrogen, A21206). For in vivo immunofluorescence, mice were euthanized and perfused with ice-cold PBS followed by 4% paraformaldehyde. Brains were dissected, soaked in 4% PFA for 24 h, then transferred to 30% sucrose for dehydration for 1 week. Then 8-µm coronal sections were made with a cryostat, including the tumour and peritumoral regions in the right striatum. Slices were permeabilized with permeabilization/wash buffer (BD Biosciences, 554723) before immunofluorescence staining. Images were captured on a Leica DMi8 inverted microscope using LasX software to perform tile scans. Nine-panel tile scans were performed on each well of 96-well plates from in vitro experiments. For in vivo immunofluorescence image capture, stained sections were imaged by 4–9 panel tile scans with LasX software. Tile scans for pMLKL were performed within the GL261 tumour region, which was identified by luciferase expression and confirmed by extremely high DAPI density. Images were quantified using Qupath positive cell detection and subcellular point detection (ASC) algorithms. Intensity thresholds were applied uniformly across all samples, and when applicable, positivity for additional markers was manually calculated by applying uniform thresholds using the countif function on detection measurements in Microsoft Excel.

Immunofluorescence of human GBM

Multiplexed immunofluorescence and immunohistochemistry labelling was done by standard indirect staining methods (for SOX2/ANXA1) and use of the iterative indirect immunofluorescence imaging (4i) protocol described previously[65] (for OLIG2/ANXA1 and EGFRvIII/FPR1). In brief, formalin-fixed paraffin-embedded tissue sections 2 µm thick were mounted on adhesive glass slides in an adaptable chamber system (Ibidi sticky slides, 80808) before deparaffinization and heat-induced antigen retrieval at pH 9. Standard indirect immunofluorescence staining included: DAPI staining (Carl Roth, 28718-90-3; 1:1,000); SOX2 (Cell Signaling Technology, 3579; 1:5,000); GFAP (Abcam 13970; 1:1,000); and ANXA1 (Abcam, ab214486; 1:2,000). For 4i, each immunofluorescence imaging cycle consisted of blocking, indirect immunofluorescence staining and DAPI staining (Carl Roth, 28718-90-3, 1:1,000), imaging on a Keyence BZ- X810 compact fluorescence microscope (Keyence Corporation) in imaging buffer and antibody elution. After five iterations, subsequent immunohistochemistry for EGFRvIII and GFAP, as well as haematoxylin counterstaining, were done adhering to the standard operating procedures of the Institute of Neuropathology in Freiburg using the same sections and performing stepwise bright-field imaging at identical locations on the same microscope. Immunofluorescence and immunohistochemistry images (with inverted grey-scale intensity) were aligned and integrated based on nuclear staining in DAPI and haematoxylin. This resulted in a 15-plexed source file for downstream analysis of each sample, created in Image J (v.1.53t with Java 1.8.0_345 (64-bit)). Antibodies used in cycle 1 were: GFAP (DAKO, Zo334; 1:1000); Iba1 (Synaptic Systems, 234308); the cycle 2 antibodies were: ANXA1 (Abcam, ab214486; 1:2,000); FPR1 (Abcam, ab113531; 1:100); cycle 3: the antibody was FPR3 (BioTechne, MAB3896; 1:500); cycle 4: the antibody was FPR2 (Santa Cruz, sc-57141; 1:200); and cycle 5: antibodies were EFGRvIII (Biozol, 31-1305-00; 1:100), GFAP (DAKO, Z0334; 1:100) and haematoxylin. In a separate cohort of six newly diagnosed GBM samples, GFAP (DAKO, Zo334; 1:1,000), ANXA1 (Abcam, ab214486; 1:2,000) and OLIG2 (Merck Millipore, MABN50; 1:1,000) were applied in a 4i panel on cycle 2. Image analysis and fluorescence quantification were done using QuPath (v.0.3.2 with Java 16.0.2). In brief, comprehensive training of automated analysis tools was carried out across samples. First, regions of interest were restricted to parenchymal/tumoral regions by training a pixel classifier to exclude erythrocyte-filled luminal endothelium and other areas of obviously unspecific antibody binding (identified by exact signal correlation across more than two channels). Next, automated segmentation was done using the Watershed cell detection algorithm anchored on a DAPI nuclear signal. Cell classification was done with a semi-supervised learning approach by using the train object classifier algorithm, whereby positive or negative cells were manually selected while confirming the accuracy of the classifier on the total image. GFAP was used to identify tumour cells and astrocytes, and IBA1 for myeloid cells. To distinguish between malignant cells and non-malignant astrocytes, we trained an object classifier to detect cells positive for GFAP and ANXA1 but not EGFRvIII, or positive for GFAP, EGFRvIII and FPR1. Detection measurements were then exported, converted to fcs format (flowCore package) and analysed in FlowJo (v.10.9.0) and R. To further filter out misclassified tumour cells, thresholding was performed in FlowJo by using the EGFRvIII signal and the nuclear:cytoplasm ratio in comparison with a healthy control sample. The number of specific detections was then divided by the surface area of the analysed region of interest and plotted against the patient's survival in days.

Multivariate survival analysis of TCGA and GLASS data

The ANXA1$^+$ astrocyte and FPR1$^+$ GBM gene expression signatures were derived from published scRNA-seq data by comparing expressing and not-expressing cells using the Seurat function FindMarkers[11]. We validated the association of our FPR1$^+$ gene expression signature with survival using data from a 2013 TCGA glioblastoma cohort[66] and the 2019 GLASS cohort[67]. Bulk RNA-seq transcripts per million and clinical data were downloaded from cBioPortal[68]. We used GenePattern's implementation of ssGSEA[69] to score enrichment of the FPR1$^+$ signature for each patient in the cohort possessing RNA-seq transcripts per million, in a cell type-specific manner, focusing on malignant cells deconvolved using Bayes prism[70]. We tested the association between signature enrichment scores and survival using Cox proportional hazards regression. The regression controlled for several clinical covariates, specifically age, temozolomide treatment status, MGMT methylation status and gene-expression subtype annotation[71]. We encoded the gene-expression subtype categorical variable by letting the mesenchymal subtype serve as reference; the remaining subtypes were represented with boolean values. For the purposes of regression, we standardized the ssGSEA scores to mean zero and unit variance. We restricted our analysis to IDH1wt patients with no missing covariates, yielding $n = 141$ patients. The regression produced an estimated hazard ratio of 1.36 ($P = 0.01$).

Flow cytometry

For flow-cytometry analysis, single-cell suspensions were obtained from the CNS as described above. The sample was first stained for 12 min at room temperature with LIVE/DEAD Fixable Aqua or Far Red Dead Cell Stain Kit (Thermo Fisher Scientific, L34966) at 1:2,500 dilution and anti-CD16/CD32 Fc block (BD Biosciences, 553142), then washed in 0.5% BSA and 2 mM EDTA pH 8.0 in PBS (FACS buffer), and then stained extracellularly with a mix of fluorescently labelled antibodies in FACS buffer for 30 min at 4 °C, protected from light. For intracellular staining, cell pellets were fixed and permeabilized following the protocols of BD Cytofix/Cytoperm (BD Biosciences, 554715) for intracellular staining. Finally, samples were washed with FACS buffer and analysed on a BD FACSymphony Analyzer (BD Biosciences). Data were analysed using FlowJo (v.10.9.0). Antibodies for T cell analysis were used at 1:100 dilution unless otherwise specified: BUV496 anti-SLAMF6 (BD Biosciences, 750046), BUV563 anti-CD11b (BD Biosciences, 741242), BUV661 anti-CD45 (BD Biosciences, 612975; 1:500), BUV737 anti-PD-1 (BD Biosciences, 749306), BUV805 anti-LAG-3 (BD Biosciences, 748540), BUV650 anti-CD3 (BD Biosciences, 740530), BV711 anti-TIGIT (BD Biosciences, 744214), BV750 anti-TNF (BD Biosciences, 566365), BV786 anti-TIM3 (BD Biosciences, 747621), FITC anti-CD8a (Biolegend, 100804), PE anti-CTLA4 (Biolegend, 106306) or BV421 anti-CTLA4 (Biolegend, 106312), PE/Dazzle 594 anti-IL-10 (Biolegend, 505034), PE/Cy5 anti-IL2 (Biolegend, 503824), PE/Cy7 anti-CD4 (Biolegend, 100422), AF700 anti-CD39 (Invitrogen, 56-0391-82) and APC/Cy7 anti-IFNγ (BD Biosciences, 561479). GL261-specific $CD8^+$ T cells were stained with an APC-conjugated H-2D(b) tetramer loaded with GARC-177-85 peptide (AALLNKLYA) (NIH Tetramer Core; 1:50 dilution). Antibodies used were: BV421 anti-CD11a (BD Biosciences, 740020; 1:20 dilution), BV605 anti-CX3CR1 (Biolegend, 149027), BV650 anti-CD11b (BD Biosciences, 563402), BV711 anti-CD8a (BD Biosciences, 752634), BV785 anti-Ly6C (Biolegend, 128041), FITC anti-CD3 (Biolegend, 100204), PE/Cy7 anti-CD4 (Biolegend, 100422), APC anti-CD45 (Thermo Fisher Scientific, 17-0451-83) and APC/Cy7 anti-CD49d (Biolegend, 103635; 1:20 dilution). CD4 T cells were sorted as $Live^+$ $CD45^+$ $CD11b^-$ $CD3^+$ $CD4^+$, CD8 T cells as $Live^+$ $CD45^+$ $CD11b^-$ $CD3^+$ $CD8^+$ cells, microglia as $Live^+$ $CD45^+$ $CD11b^+$ $Ly6C^{low/-}$ $CX3CR1^+$ $CD49d^{low}$, $CD11a^{low}$. Monocytes were sorted as $CD45^+$ $CD11b^+$ $Ly6C^{high}$ $CD49d^{high}$ $CD11a^{high}$. Cells were sorted using a FACSAria IIU (BD Biosciences).

FACS sorting

Cell suspensions were stained extracellularly as described above with Live/Dead stain and Fc block, and finally with a mix of antibodies in FACS buffer for 30 min at 4 °C. All antibodies were diluted 1:100 in FACS buffer. Before sorting, cell suspensions were filtered through tubes with 35-µm cell strainer caps (Falcon, 352235). For RNA-seq analyses, cells were sorted directly into 100 µl Picopure Extraction Buffer (Thermo Fisher Scientific, KIT0204), incubated 30 min at 42 °C and then stored at −80 °C until RNA isolation and sequencing was done.

FACS analysis of T cells

To analyse tumour-infiltrating T cells by flow cytometry, magnetic-activated cell separation was used to negatively select T cells with the Pan T Cell Isolation Kit II mouse (Miltenyi Biotec, 130-095-130) following the manufacturer's protocol. T cell culture medium was composed of RPMI 1640 (Gibco, 11875119) supplemented 10% FBS, 1% penicillin/streptomycin, 50 µM 2-mercaptoethanol (Sigma-Aldrich, M6250), 1% non-essential amino acids (Thermo Fisher Scientific, 11140050), 10 mM HEPES (Thermo Fisher Scientific, 15630130), 1 mM sodium pyruvate (Thermo Fisher Scientific, 11360070) and 1× GlutaMAX (Thermo Fisher Scientific, 35050061). Collected T cells were then reactivated in culture medium supplemented with 50 ng ml^{-1} phorbol 12-myristate 13-acetate (PMA) (Sigma Aldrich, P8139), 1 µM ionomycin (Sigma Aldrich, I3909-1ML) and 1:1,500 of each GolgiStop and GolgiPlug (BD Biosciences, 554724) for 4 h at 37 °C. T cells were then incubated with 50 nM dasatinib (Selleck Chemicals, S1021) and 1:200 FcBlock (BD Biosciences: 553142) for 20 min at 37 °C. To this solution, APC-conjugated H-2D(b) tetramer loaded with GARC-$1_{77–85}$ peptide (AALLNKLYA) (NIH Tetramer Core) was added for a final dilution of 1:50 in 2% FBS and incubated at room temperature for 1 h in the dark. Washing was performed with FACS buffer and centrifugation at 600*g* for 5 min at 4 °C. Next, surface markers were stained in FACS buffer for 30 min at 4 °C, followed by cell fixation and permeabilization with BD Cytofix/Cytoperm (BD Biosciences, 554715) for 20 min at 4 °C according to the manufacturer's protocol. Intracellular markers and cytokines were stained with antibodies diluted in permeabilization buffer. Finally, stained T cells were stored at 4 °C in FACS buffer until cytometric analysis.

Bioinformatic analysis

Bulk RNA-seq expression of *Fpr1*, *Fpr2* and *Fpr3* in GL261 cells was quantified as previously described[72]. Spatial transcriptomic data of *ANXA1* and *FPR1* in glioblastoma were analysed from previously published datasets[15]. Single-cell RNA-seq samples were aligned to GRCm38 reference genome and GRCh38 reference genome and were quantified using the STARsolo function in STAR software[73], respectively. To call malignant cells, the gene expression matrix was analysed by CONICsmat[74]. The copy number variations of each chromosome arm were calculated for each cell, and the malignant cells were called based on gain of chromosome 7 and loss of chromosome 10. Non-malignant cells identified by copy-number variation analysis were reclustered and cell types were called using unbiased cell-type recognition singleR[75] and confirmed by canonical marker expression. To obtain the biological relevance score, the genes that were differentially expressed in astrocytes between different recurrence states were obtained from a previously published scRNA-seq dataset[11] Differentially expressed genes were analysed using the enrichment analysis of the ClusterProfiler package[76], and their occurrences in all pathways were counted. Then the top genes that were enriched in the most pathways were selected. The connectome of the single-cell RNA-seq samples were generated using the pipeline published with the Rabid-Seq protocol[3,76]. In the human GBM RABID-seq dataset, multiple samples were obtained from multiple donors, and rabies barcode detection and connection calling was done on each donor sample to avoid false-positive connectivity between different samples from different donors. Seurat (v.4.3)[77] was used to perform the analysis. Empty droplets were detected and removed using the EmptyDrop algorithm[78,79]. Cells with mitochondrial contents higher than 25% were removed. The batch effects between different samples were corrected using harmony[80] and clustered using Louvain community clustering[77]. For human RABID-seq UMAP representation, 12 or 14 principal components were used for all cells and for non-malignant cells, respectively. Signature scores used in the paper were calculated using the algorithm described previously[77,81]. A necroptosis-related gene signature was obtained from ref. 28. All differential expression analyses in this manuscript were performed on the log-transformed counts-per-million normalized expression of cells. Thus, any potential differences caused by library size and sequencing depth were mitigated. We chose Mann–Whitney–Wilcoxon ranked-sum tests for the differential-expression analyses, so that bias brought by unequal numbers of cells in different groups and unequal variances within groups were considered. Pathway analysis was done by gene-set enrichment analysis (Broad Institute, v.4.3.2) or Ingenuity Pathway Analysis (Qiagen) using a pre-ranked list with the average expression $\log_2$(FC) as the ranking metric. Curated gene signatures from the Molecular Signatures Database (MSigDB) v.2023.1 were used to identify relevant pathways. Seurat (v.4.3), dittoSeq (v.4.3), ggplot2 (v.3.5) and circlize (v.0.4.16) were used for visualization. Volcano plots were generated using EnhancedVolcano (v.3.17). We thank github.com/PeeperLab for sharing the replotGSEA function. All R-based analyses were done on RStudio (v.4.3.0) with R (v.4.3.1).

Statistical analysis

GraphPad Prism 10 (GraphPad Software, v.10.0.2) was used for visualizations and to calculate significant differences. Sample sizes (*n*) refer to biological replicates. For in vitro studies, replicates indicate independent biological samples randomly allocated into experimental groups. For in vivo studies, replicates indicate individual mice randomly allocated to experimental groups. No statistical methods were used to predetermine sample sizes. Statistical tests used to detect significant differences between groups are detailed in the figure legends for each experiment. A *P* value of less than 0.05 was considered significant.

Reporting summary

Further information on research design is available in the Nature Portfolio Reporting Summary linked to this article.

Data availability

Sequencing data have been deposited in the Gene Expression Omnibus (GEO) under the respective SuperSeries accession codes: human data, GSE263612; mouse single cell data, GSE263613; mouse bulk RNA-seq data, GL261 sg*Fprl* versus GL261 sgRandom, GSE263737; AAV sg*GFAP-Anxal* versus AAV GFAP-sg*Rosa*, GSE263738. Publicly available datasets: scRNA-seq dataset from ref. 11, https://github.com/kpetrecca/NeuroOncology2022.git; spatial transcriptomics datasets from ref. 15, https://datadryad.org/dataset/doi:10.5061/dryad.h70rxwdmj; Ivy Glioblastoma Atlas (ref. 27), http://glioblastoma.alleninstitute.org; TCGA/GLASS, http://www.cbioportal.org; GRCh38 reference genome, https://ftp.ensembl.org/pub/release-113/fasta/homo_sapiens/dna/. All other data are available from the corresponding authors upon reasonable request. Correspondence and request for materials should be addressed to F.J.Q.
Source data are provided with this paper.

61. Lee, Y., Messing, A., Su, M. & Brenner, M. GFAP promoter elements required for region-specific and astrocyte-specific expression. *Glia* **56**, 481–493 (2008).
62. Hunker, A. C. et al. Conditional single vector CRISPR/SaCas9 viruses for efficient mutagenesis in the adult mouse nervous system. *Cell Rep.* **30**, 4303–4316 (2020).
63. Challis, R. C. et al. Systemic AAV vectors for widespread and targeted gene delivery in rodents. *Nat. Protoc.* **14**, 379–414 (2019).
64. Opitz, C. A. et al. An endogenous tumour-promoting ligand of the human aryl hydrocarbon receptor. *Nature* **478**, 197–203 (2011).
65. Gut, G., Herrmann, M. D. & Pelkmans, L. Multiplexed protein maps link subcellular organization to cellular states. *Science* **361**, eaar7042 (2018).
66. Brennan, C. W. et al. The somatic genomic landscape of glioblastoma. *Cell* **155**, 462–477 (2013).
67. Barthel, F. P. et al. Longitudinal molecular trajectories of diffuse glioma in adults. *Nature* **576**, 112–120 (2019).
68. Cerami, E. et al. The cBio cancer genomics portal: an open platform for exploring multidimensional cancer genomics data. *Cancer Discov.* **2**, 401–404 (2012).
69. Barbie, D. A. et al. Systematic RNA interference reveals that oncogenic *KRAS*-driven cancers require TBK1. *Nature* **462**, 108–112 (2009).
70. Chu, T., Wang, Z., Pe'er, D. & Danko, C. G. Cell type and gene expression deconvolution with BayesPrism enables Bayesian integrative analysis across bulk and single-cell RNA sequencing in oncology. *Nat. Cancer* **3**, 505–517 (2022).
71. Verhaak, R. G. W. et al. Integrated genomic analysis identifies clinically relevant subtypes of glioblastoma characterized by abnormalities in PDGFRA, IDH1, EGFR, and NF1. *Cancer Cell* **17**, 98–110 (2010).
72. Maire, C. L. et al. Glioma escape signature and clonal development under immune pressure. *J. Clin. Invest.* **130**, 5257–5271 (2020).
73. Dobin, A. et al. STAR: ultrafast universal RNA-seq aligner. *Bioinformatics* **29**, 15–21 (2013).
74. Müller, S., Cho, A., Liu, S. J., Lim, D. A. & Diaz, A. CONICS integrates scRNA-seq with DNA sequencing to map gene expression to tumor sub-clones. *Bioinformatics* **34**, 3217–3219 (2018).
75. Aran, D. et al. Reference-based analysis of lung single-cell sequencing reveals a transitional profibrotic macrophage. *Nat. Immunol.* **20**, 163–172 (2019).
76. Zorita, E., Cuscó, P. & Filion, G. J. Starcode: sequence clustering based on all-pairs search. *Bioinformatics* **31**, 1913–1919 (2015).
77. Satija, R., Farrell, J. A., Gennert, D., Schier, A. F. & Regev, A. Spatial reconstruction of single-cell gene expression data. *Nat. Biotechnol.* **33**, 495–502 (2015).
78. Lun, A. T. L. et al. EmptyDrops: distinguishing cells from empty droplets in droplet-based single-cell RNA sequencing data. *Genome Biol.* **20**, 63 (2019).
79. Griffiths, J. A., Richard, A. C., Bach, K., Lun, A. T. L. & Marioni, J. C. Detection and removal of barcode swapping in single-cell RNA-seq data. *Nat. Commun.* **9**, 2667 (2018).
80. Korsunsky, I. et al. Fast, sensitive and accurate integration of single-cell data with Harmony. *Nat. Methods* **16**, 1289–1296 (2019).
81. Tirosh, I. et al. Dissecting the multicellular ecosystem of metastatic melanoma by single-cell RNA-seq. *Science* **352**, 189–196 (2016).

Acknowledgements We thank all Quintana lab members for discussion related. This work was supported by grants NS102807, ES02530, ES029136 and AI126880 from the NIH; RG4111A1 and JF2161-A-5 from the NMSS; RSG-14-198-01-LIB from the American Cancer Society; and PA-1604-08459 from the International Progressive MS Alliance. B.M.A. was supported by the Training Program in Nervous System Tumors (K12CA090354) from NCI/NIH; the Career Enhancement Program (CEP) for the NCI/NIH SPORE at Harvard Cancer Center (P50CA165962) from NCI/NIH; the Post-Doctoral Fellowship in Translational Medicine from the PhRMA Foundation; Cancer Neuroscience grant T32CA272386 from NCI/NIH; and 1IK2BX006568-01A1 from the Department of Veterans Affairs, Veterans Health Administration, Office of Research and Development, Biomedical Laboratory Research and Development. C.F.A. was supported by a scholarship from the German Academic Exchange Service (DAAD). M.D. was supported by the Swiss National Science Foundation (project number 199310) and the German Research Foundation (IMM-PACT-programme, 413517907). L.F. was funded by the Gemeinnützige Hertie-Stiftung (medMS-Doktorandenprogramm). M.A.W. was supported by NINDS, NIMH, NIDA and NCI (R01MH130458, R00NS114111, T32CA20720, R01MH132632 and R01DA061199). J.-H.L was supported by the Basic Science Research Program funded by the National Research Foundation of Korea (NRF)/Ministry of Education (2022R1A6A3A03071157), and a long-term postdoctoral fellowship funded by the Human Frontier Science Program (LT0015/2023-L). T.I. was supported by an EMBO postdoctoral fellowship (ALTF, 1009-2021). H.-G.L. was supported by a Basic Science Research Program through the National Research Foundation of Korea (NRF) funded by the Ministry of Education (2021R1A6A3A14039088). K.L.L. was supported by NCI/NIH SPORE at Harvard Cancer Center P50CA165962. C.M.P. was supported by the National Multiple Sclerosis Society (FG-2307-42209) and the Mayer Foundation. We thank R. Krishnan for technical assistance with flow cytometry and FACS; L. Ding at the Brigham and Women's Hospital NeuroTechnology Studio (NTS) for technical assistance with confocal microscopy; staff at the NTS for use of their 10× Chromium controller; K. Grieco and S. Valentin, the BWH pathologist assistants and staff at the Tissue and Blood Repository for tissue support.

Author contributions B.M.A., C.F.A., M.A.W., D.A.R., E.A.C. and F.J.Q. designed the study. B.M.A., C.F.A., M.K., J.M.R., A.M., J.E.K., J-H.L., H-G.L., C.M.P., L.G., G.P., T.I., J.J.Y., A.G., J.M., E.N.C., L.S., D.F., L.E.F., A.M.S., L.M.S., F.G., M.C., C.G-V. and R.N. performed or assisted with in vitro and in vivo experiments. K.L.L., E.A.C., D.A.R., M.M.C., E.L., C.C.B. and P.S.P. provided neuropathology expertise, tissue resources and patient models. M.P., M.D. and L.F. performed GBM multiplex immunofluorescence. Z.L. and C.F.A. performed bioinformatic analysis. D.M., J.H.W., and G.G. performed multivariate survival analyses. B.M.A., C.F.A. and F.J.Q. wrote the manuscript with input from co-authors. F.J.Q. directed and supervised the study.

Competing interests F.J.Q and M.A.W have filed a provisional patent regarding the RABID-seq technology used in this paper. The remaining authors declare no competing interests.

Additional information

Supplementary information The online version contains supplementary material available at https://doi.org/10.1038/s41586-025-09191-9.

Correspondence and requests for materials should be addressed to Francisco J. Quintana.

Peer review information *Nature* thanks Michael Platten and the other, anonymous, reviewer(s) for their contribution to the peer review of this work.

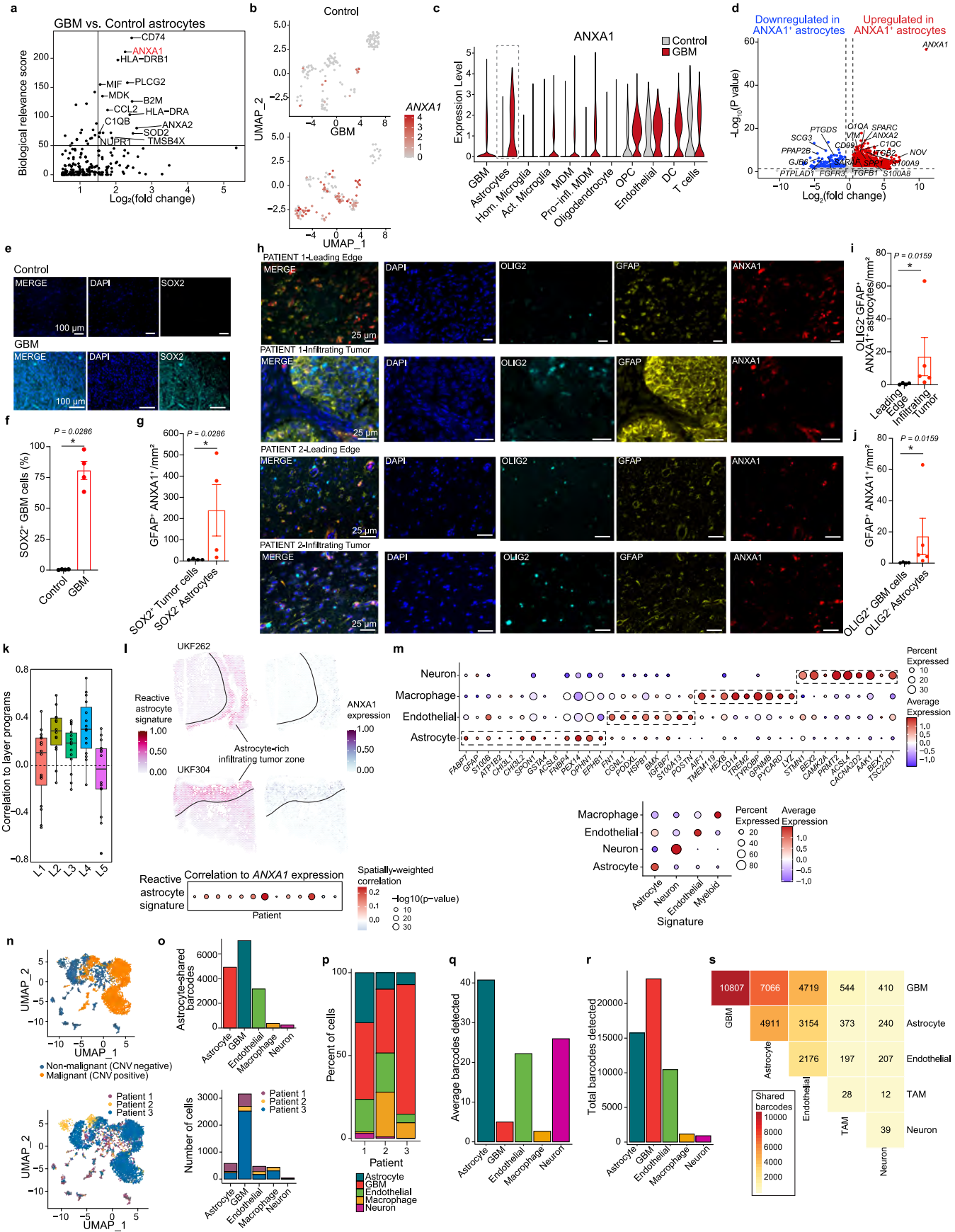

Extended Data Fig. 1 | See next page for caption.

Extended Data Fig. 1 | scRNA-seq, spatial transcriptomic, and ptRABID-seq analysis of astrocytes in GBM. (**a**) Biological relevance score of astrocyte DEGs; GBM vs. controls[11]. (**b**) Feature plot of *ANXA1* in control and GBM scRNA-seq astrocytes. (**c**) Violin plot of *ANXA1* expression by cell type in control and GBM. (**d**) Volcano plot of DEGs between *ANXA1*$^+$ and *ANXA1*$^-$ astrocytes in human GBM scRNA-seq. (**e**) Control and GBM specimen staining of SOX2 to identify malignant cells. (**f**) Quantification of SOX2$^+$ cells in control and GBM specimens. (n = 4 specimens each; p = 0.0286 by two-sided unpaired Mann-Whitney U-test). (**g**) ANXA1$^+$ tumor cell (GFAP$^+$ SOX2$^+$) and astrocyte (GFAP$^+$SOX2$^-$) density at the infiltrating tumor zone (ITZ). Each point represents a separate brain, (n = 4 specimens each; p value from Mann-Whitney U-test). (**h**) ANXA1 staining in astrocytes in n = 5 GBMs in which malignant cells are distinguished by OLIG2 staining. Regions adjacent to tumor core (ITZ) were compared with regions distant from the tumor (leading edge; LE) when available. (**i**) ANXA1$^+$ astrocyte density at LE vs. ITZ, using OLIG2 as a tumor marker. In total, n = 3,641 GBM-associated astrocytes at the ITZ and n = 1,213 GBM-associated astrocytes at the LE; two-tailed unpaired U-test. (**j**) ANXA1$^+$ tumor cell (GFAP$^+$ OLIG2$^+$) and astrocyte (GFAP$^+$OLIG2$^-$) density at the ITZ. p = 0.0159 by Mann-Whitney U-test. (**k,l**) Spatial transcriptomics of the reactive astrocyte gene signature correlated to spatially defined layers programs (k) and to *ANXA1* expression (l) in n = 13 GBMs. (**m**) Dot plot (top) and signature score (bottom) of cell type markers of cells analyzed by ptRABID-seq (n = 1,520 cells). (**n**) UMAP of CNV analysis (top, n = 3,157 malignant and 1,520 non-malignant cells), and cells grouped by patient (bottom) in ptRABID-seq. (**o**) Number of barcodes shared between astrocytes and other cell types (top) and divided by patient (bottom), as detected by RABID-seq. **(p)** Proportions of cell types in ptRABID-seq. (**q, r**) Average (q) and total (r) barcode numbers detected in each cell type in ptRABID-seq. (**s**) Shared barcodes between each cell type in ptRABID-seq. Data are mean and error bars show ± SEM (**f, g, i, j**).

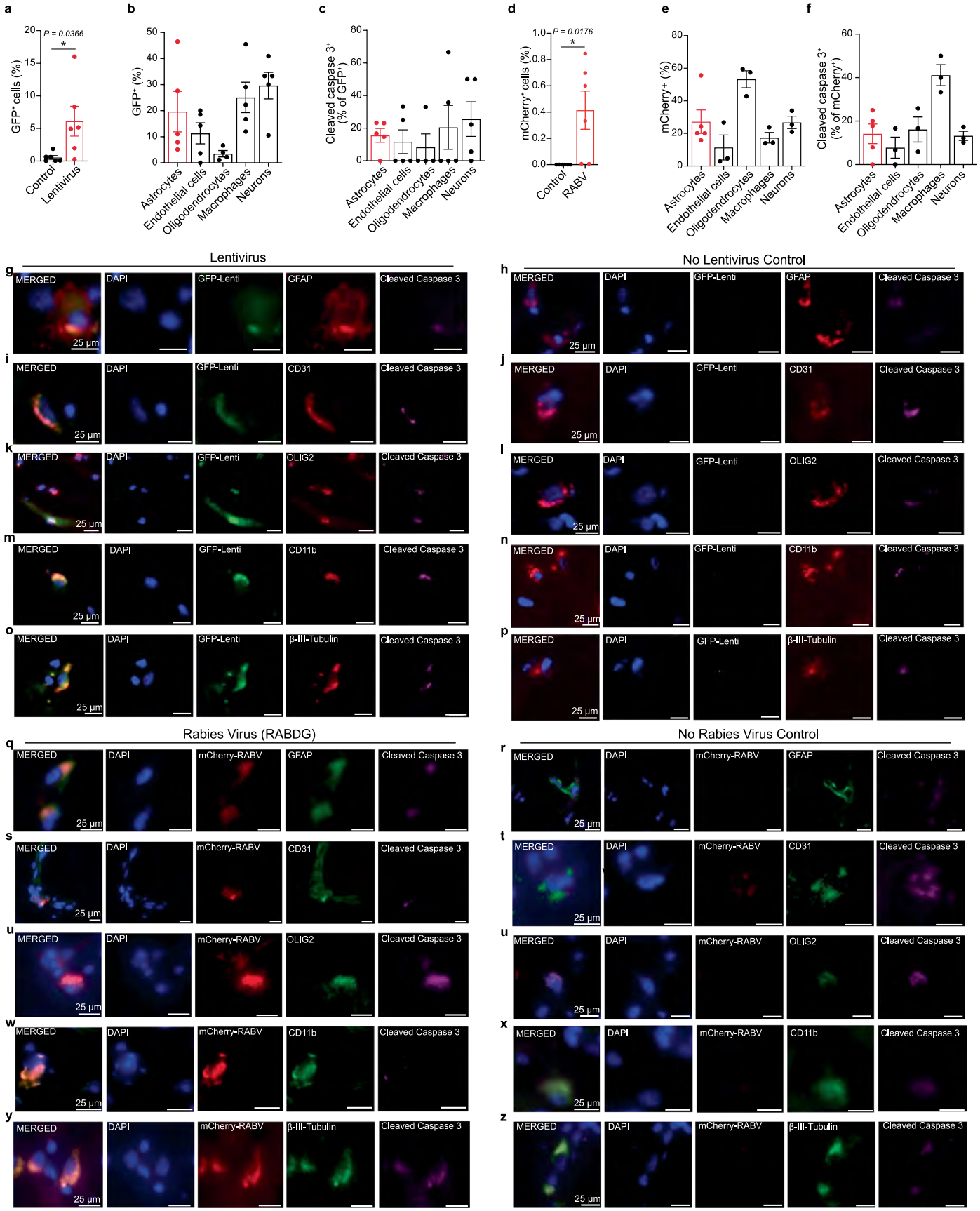

Extended Data Fig. 2 | See next page for caption.

Extended Data Fig. 2 | Detection of lentivirus transduction and rabies virus infection in human organotypic cultures. (**a**) Quantification of GFP^+ staining (indicating transduction by the helper lentivirus that delivers TVA and G) as determined by brightfield immunofluorescence detection (each dot represents a separate culture, and n = 6 organotypic cultures per condition from epilepsy surgery (non-GBM)). (**b**) Quantification of GFP^+ cells by cell type. Each slide was co-stained for GFP, DAPI, and one cell type marker. Each dot represents a separate culture, and n = 5 organotypic cultures per condition from epilepsy surgery. (**c**) Quantification of apoptotic GFP^+ cells by cell type using cleaved caspase-3 as a marker of apoptosis. Each slide was co-stained for GFP, one cell type marker, and cleaved caspase 3. Each dot represents a separate culture, and n = 5 organotypic cultures per condition from epilepsy surgery (non-GBM). (**d**) Quantification of $mCherry^+$ staining (indicating rabies infection) as determined by brightfield immunofluorescence detection. Each dot represents a separate culture, and n = 6 organotypic cultures per condition. (**e**) Quantification of $mCherry^+$ cells by cell type. Each slide was co-stained for mCherry, DAPI, and one cell type marker. Each dot represents a separate culture, and n = 5 organotypic cultures for astrocytes, n = 3 cultures for other cell types. (**f**) Quantification of apoptotic $mCherry^+$ cells by cell type using cleaved caspase 3 as a marker of apoptosis. Each slide was co-stained for DAPI, mCherry, one cell type marker, and cleaved caspase 3. Each dot represents a separate culture, and N = 5 organotypic cultures for astrocytes and n = 3 for other cell types. **(g-p)** Representative images of control and lentivirus transduced cultures. **(q-z)** Representative images of control and rabies virus-infected cultures. Data are mean and error bars show ± SEM (**a-f**).

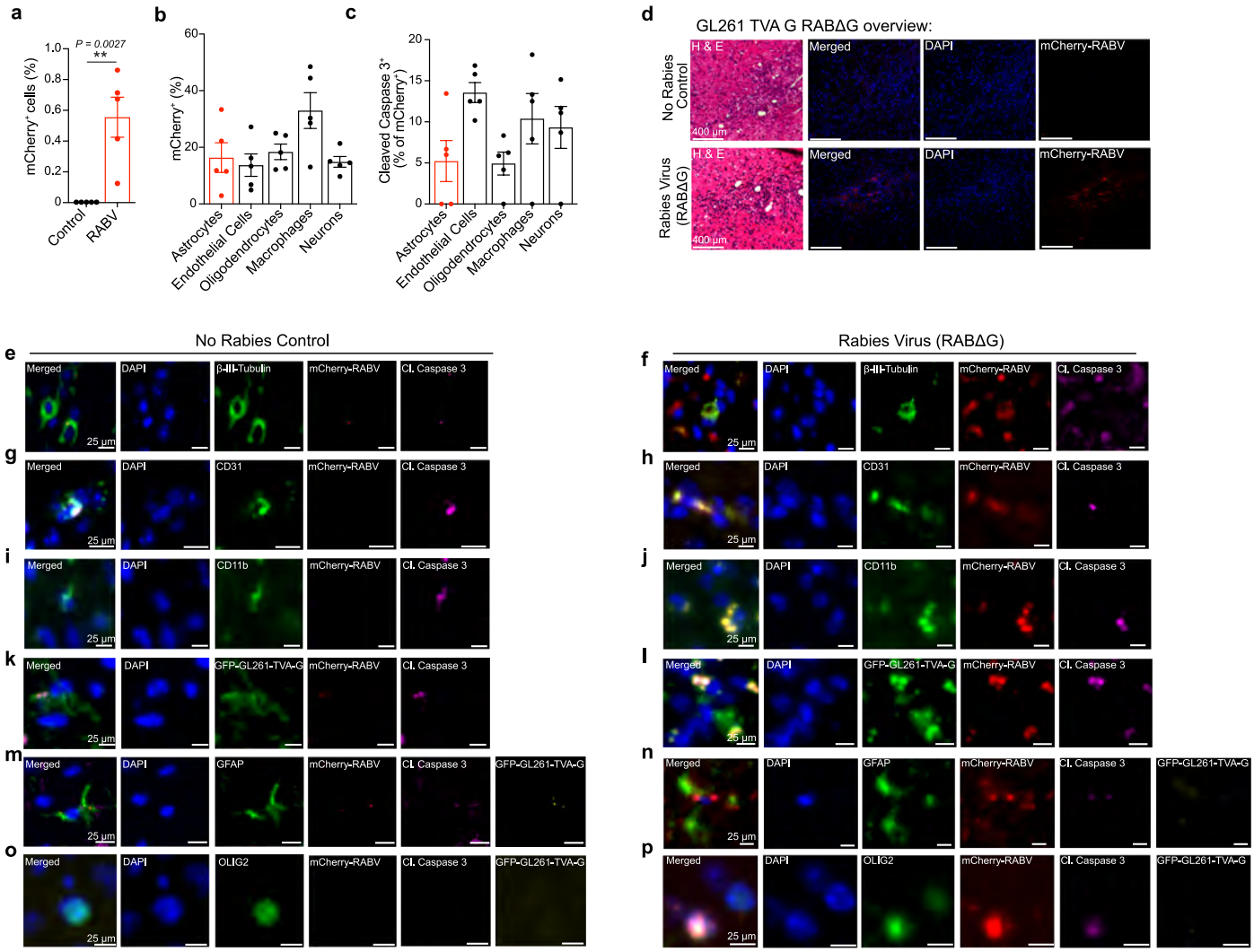

Extended Data Fig. 3 | Analysis of tumor-anchored RABID-seq. GL261-TVA-G bearing mice were injected with 1,000 infectious units of rabies one week after tumor implantation; GL261-TVA-G bearing mice were used as controls (n = 5 each). **(a-c)** Quantification of total (a), cell-type specific (b) mCherry$^+$ staining (indicating rabies infection), and cleaved caspase-3$^+$ staining of mCherry$^+$ cells (c) as determined by brightfield immunofluorescence detection. Each dot represents one animal, and in **a**, statistics were two sided unpaired t-test. **(d)** Overview images of control non-rabies injected tumor site (top) and rabies injected tumor site (bottom) from representative animals. Hematoxylin and eosin (H&E) reference images are taken from slices proximate to the immunofluorescence slices for reference purposes. **(e-p)** Representative images of rabies-injected and control staining by cell type. GFP-negative cells were used as controls when staining for GFAP and OLIG2 to exclude malignant cells. Data are mean and error bars show ± SEM (**a-c**).

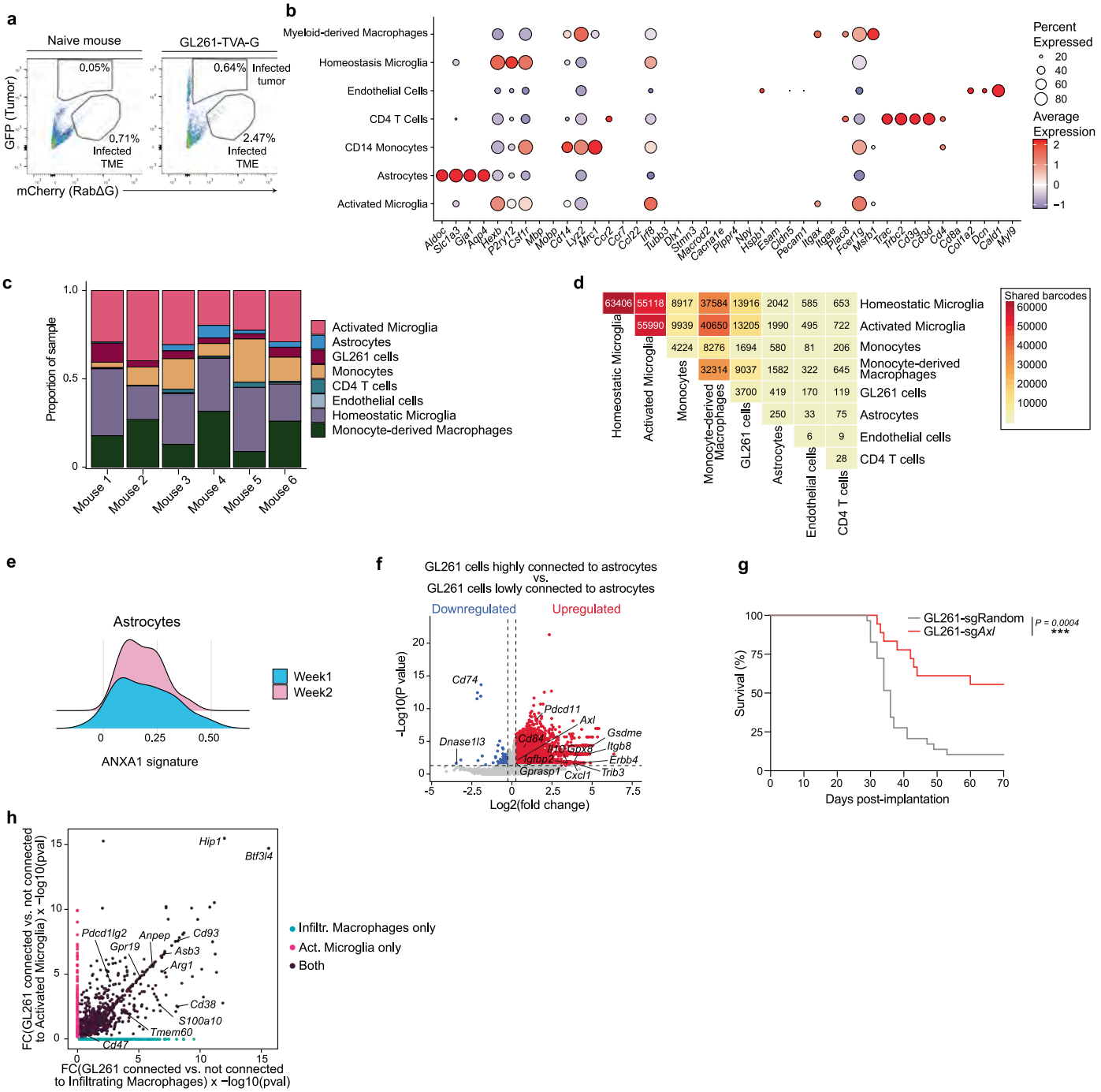

Extended Data Fig. 4 | Tumor-anchored RABID-seq identifies regulators of glioma-TME interactions. (**a**) Representative FACS plot of cells isolated from GL261-anchored RABID-seq one week after infection. (**b**) Dot plot showing cell type markers used for identification of cell types captured by taRABID-seq (n = 6 mice and 21,189 cells). (**c**) Cell type proportions by analyzed mouse sample. (**d**) Matrix showing shared barcodes between each cell type. (**e**) *Anxa1* signature in mouse astrocytes isolated 14 or 21 days after tumor implantation. (**f**) Volcano plot showing DEGs of GL261 cells highly connected to astrocytes vs. lowly connected to astrocytes, with immunosuppression-related genes of interest labeled. (**g**) Kaplan-Meier plot of GL261 bearing mice with gRNA targeting *Axl* or a random gRNA sequence (n = 26 mice sgRandom and n = 16 mice sg*Axl*; p calculated from log-rank analysis; represents 3 pooled experiments). (**h**) Scatter plot of gene expression correlation between GL261 connected vs. not connected to activated microglia, by GL261 connected vs. not connected with infiltrating monocyte-derived macrophages.

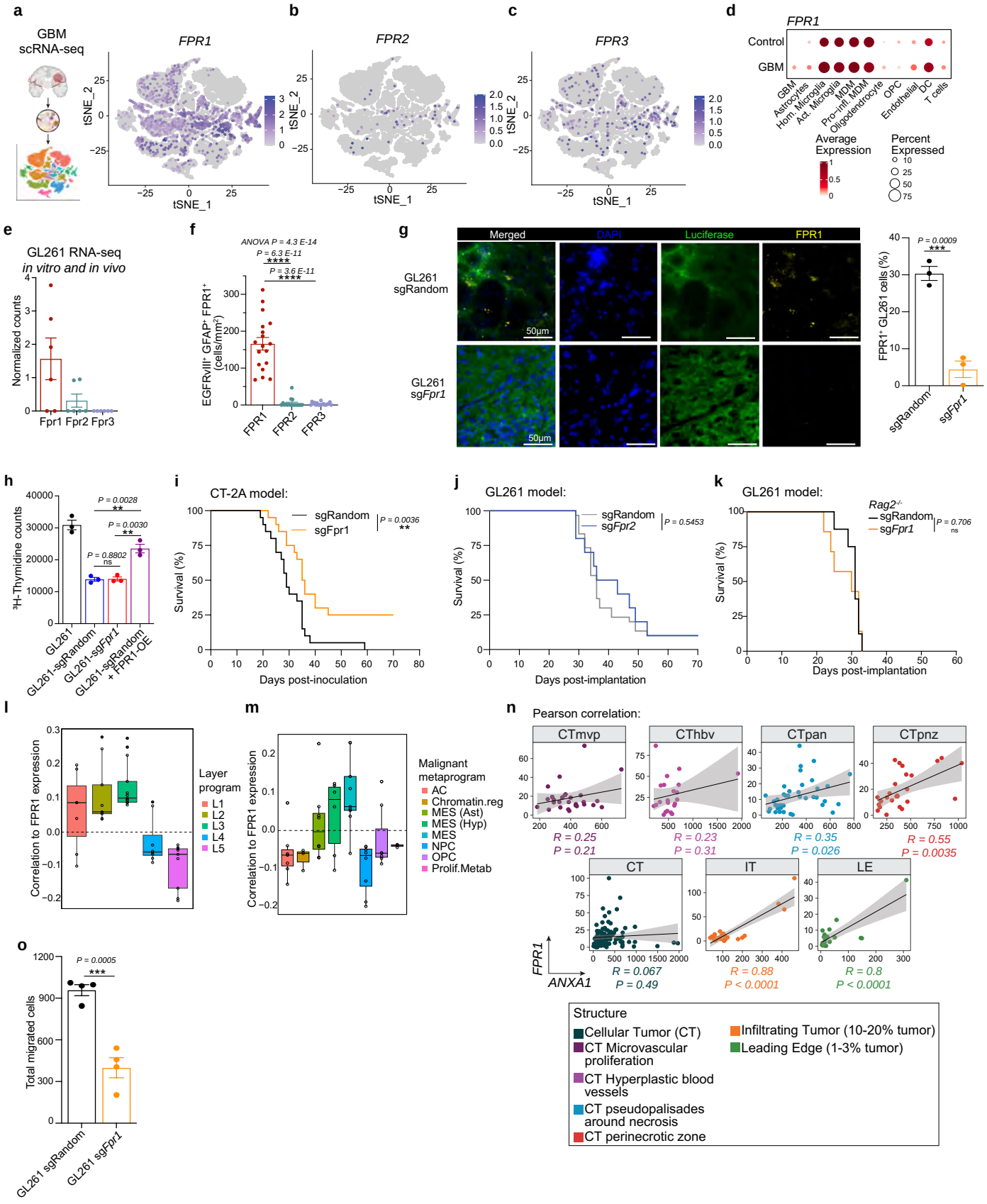

Extended Data Fig. 5 | See next page for caption.

Extended Data Fig. 5 | FPR expression in GBM and survival. (**a-c**) *FPR1* (a), *FPR2* (b), and *FPR3* (c) in a GBM scRNA-seq dataset[11] (n = 25 patients). (**d**) Dot plot of *FPR1* by cell type in GBM scRNA-seq data[11]. (**e**) RNA-seq of *Fpr1,2,3* in GL261 cells. Each dot represents a mouse or cell culture replicate. n = 3 GL261 bearing mice, n = 3 cell culture replicates per group. (**f**) *FPR1* expression in GBM cells (one dot per patient, and n = 18 patients; statistics by two-way ANOVA with Tukey's multiple comparisons test; post-hoc unpaired two tailed t-tests were then performed). (**g**) *Fpr1* inactivation in GL261-implanted mice (n = 3 mice per group; each dot represents average staining from a 9 high power field tile scan from one mouse's tumor; statistics were from two-sided unpaired t-test). (**h**) Thymidine incorporation assay of GL261 sub-lines cultured for 6 h with thymidine. P values were calculated by unpaired two-sided t-test. (**i**) Survival of mice bearing CT2A harboring *Fpr1* or random sequence gRNA (n = 20 mice per group, statistics were log rank; represents 3 pooled experiments). (**j**) Survival of mice bearing control GL261 or GL261 with *Fpr2* gRNA (n = 20 mice for sgRandom; n = 10 mice for sg*Fpr2*; statistical test by log rank; repeated twice with identical results). (**k**) Survival of *Rag2*$^{-/-}$ mice bearing GL261 harboring *Fpr1* or random control gRNA (n = 8 mice sgRandom and n = 7 sg*Fpr1* group; statistics by log rank; repeated twice with identical results). (**l**) Box and whisker plot of FPR1 expression vs. spatially defined layers programs[16]. (**m**) Box and whisker plot of FPR1 correlation to malignant metaprograms[16]. Boxplots display median, interquartile range (IQR) ± 1.5IQR and outlier values (**n**) Correlation of *FPR1* and *ANXA1* expression from the Ivy Glioblastoma Atlas[27]. (**o**) Transwell migration assay of GL261 sgRandom vs GL261 sg*Fpr1*; p value from unpaired two-tailed t-test. *** $p < 0.001$, ** $p < 0.005$. Data are mean and error bars show ± SEM (**e-h, o**). Illustrations in **a** created in BioRender (Lee, J. https://BioRender.com/0bkvepw; 2025).

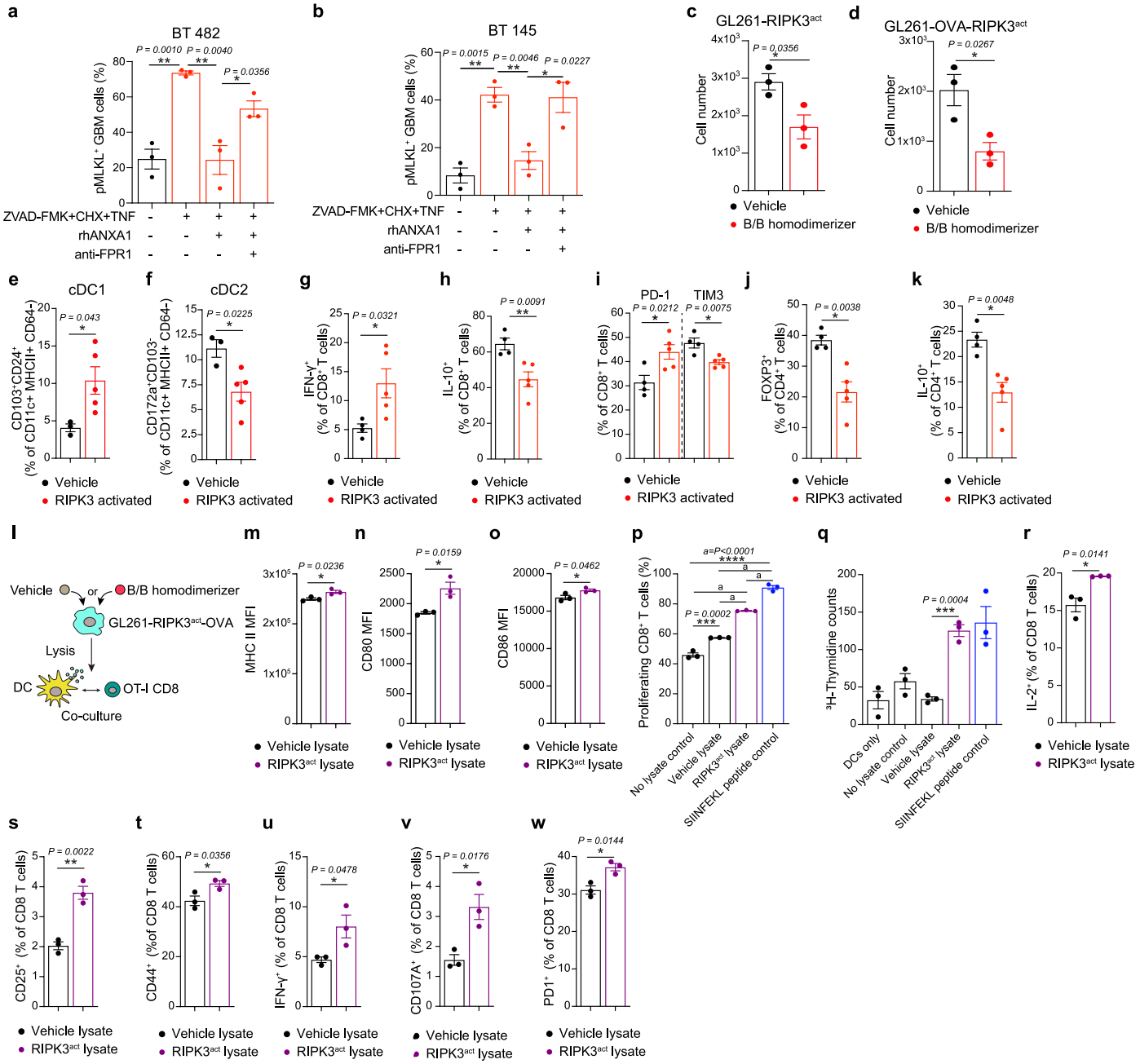

Extended Data Fig. 6 | Immune response from necroptotic GL261. (**a-b**) Immunofluorescence of pMLKL in two human GBM isolates following necroptosis induction in the presence of rhANXA1 and/or an FPR1 neutralizing antibody (each dot represents a separate well, with n = 3 wells per condition; p values were calculated by two-sided unpaired t-test and replicated twice). (**c-d**) In vitro demonstration of GL261-RIPK3^{act} (c) or GL261-OVA-RIPK3^{act} (d) cell death as measured 48 h after the addition of 50 µM B/B homodimerizer (n = 3 wells per condition; two-sided unpaired t-test; experiment was replicated 3 times). (**e-k**) Flow cytometry analysis of vehicle (n = 3) vs RIPK3-activated (n = 5 mice) GL261-infiltrating cDC1 (e), cDC2 (f;) subsets, and CD8$^+$ T cells (n = 4 and n = 5 mice) for IFN-γ (g), IL-10 (h), PD1 and TIM3 expression (I); and FOXP3 expression (j) and IL10 expression (k) in the CD4$^+$ population. Unpaired two-tailed t-test (**e-k**). (**l**) Schematic for antigen presentation assay in which lysate from RIPK3 activated or control GL261-OVA cells was pulsed onto splenic DCs, and co-cultured with transgenic SIINFEKL-specific OT1 CD8 T cells. (**m-o**) Mean fluorescence intensities of CD11c$^+$ MHCII$^+$ dendritic cells, I-a/I-e (m), CD80 (n), and CD86 (o). (**p**) Percent proliferating CD3$^+$ CD8$^+$ T cells from OT1 mice, as measured by Cell Trace dilution, after 72 h of co-culture with lysate-pulsed DCs. (**q**) Thymidine incorporation assay of co-cultures taken in the final 12 h. (**r-w**) Flow cytometry of OT1 CD8 T cells from co-culture, displaying upregulation of IL-2 (r), CD25 (s), CD44 (t), IFNγ (u), CD107a (v), and PD1 (w). n = 3 replicates per group, p values from unpaired two tailed t-test for **m-w**. Data are mean and error bars show ± SEM (**a-k; m-w**.

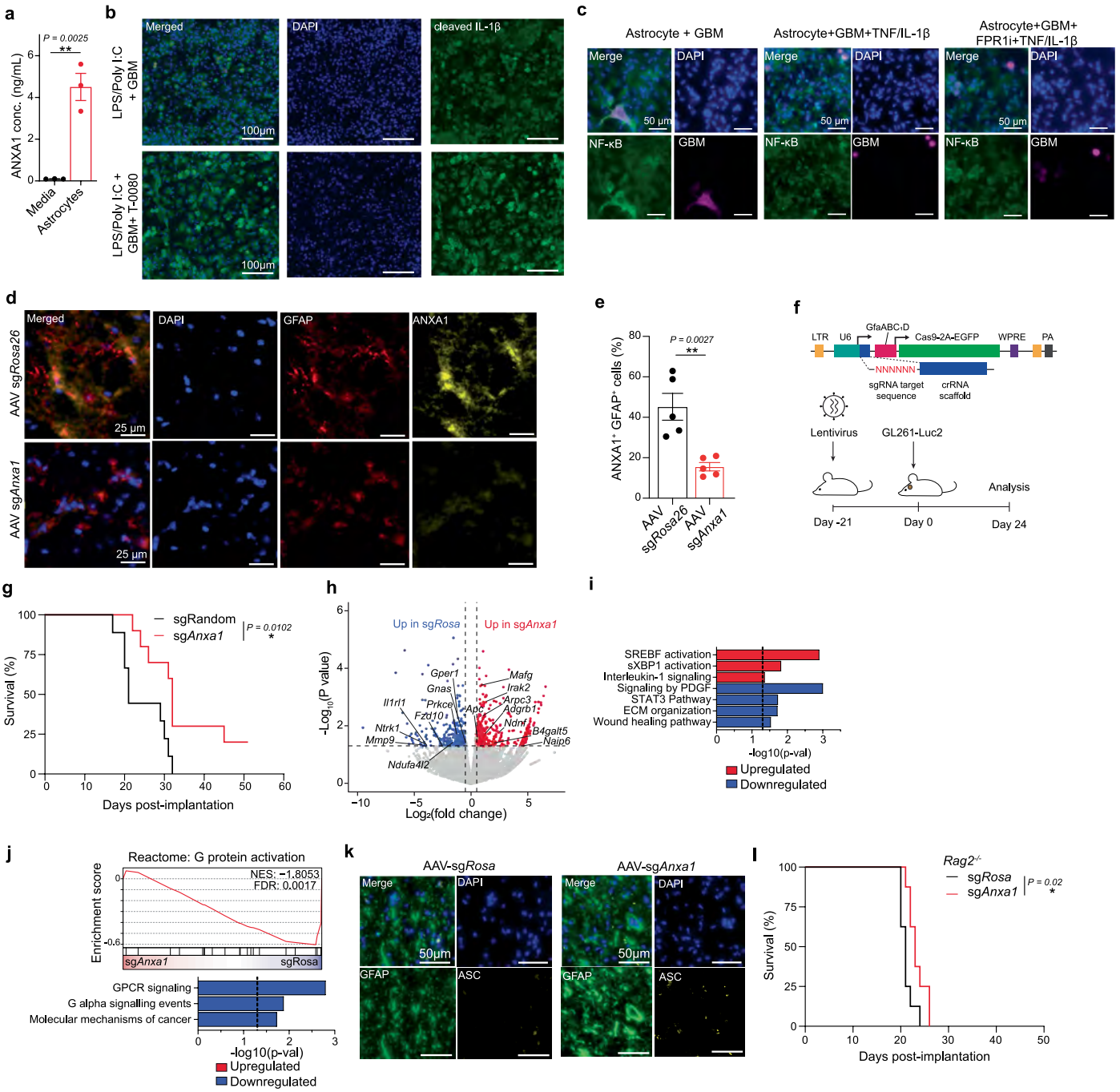

Extended Data Fig. 7 | Investigation of astrocyte ANXA1 signaling. (**a**) ELISA quantification in supernatants of primary human astrocytes (n = 3 wells per group; unpaired two-tailed t-test; graph represents one replicate experiment which was performed 3 times with similar results). (**b**) Representative images from staining of human astrocytes for cleaved IL-1β. (**c**) Representative images corresponding to Fig. 4j, detecting nuclear NF-κB in human astrocyte-GBM co-cultures. (**d-e**) Validation of astrocyte-specific *Anxa1* knockdown with AAV-PHP.eB and sgRNA. Representative image (d) and automated quantification (e) of ANXA1$^+$ cells of GFAP$^+$ astrocytes (n = 5 sg*Rosa*-transduced and n = 5 sg*Anxa1* transduced mice; p values from unpaired two-tailed t-test). (**f**) Schematic of lentivirus-mediated *Anxa1* perturbation study. (**g**) Kaplan-Meier survival plot of GL261 bearing mice following astrocyte-specific *Anxa1* inactivation with lentivirus. Transduction with a random gRNA was used as a control. (n = 9 mice for sgRandom and n = 10 mice for sg*Anxa1* group; p values from log rank; experiment was repeated twice with similar results). (**h-i**) Volcano plot (h) and ingenuity pathway analysis (IPA; i) of astrocytes from sg*Anxa1* vs. sg*Rosa* transduced mice (n = 4 sg*Anxa1* and n = 3 sg*Rosa* mice per group). (**j**) Gene set enrichment pathway analysis (GSEA) of astrocyte specific knockdown of *Anxa1* showing decreased G protein-coupled receptor signaling in GL261 cells (n = 3 sg*Rosa* and n = 4 sg*Anxa1* transduced mice). (**k**) Representative images of immunofluorescence staining of ASC, GFAP, and DAPI in peritumoral regions from GL261-bearing mice from day 24, corresponding to Fig. 4n. (**l**) Kaplan-Meier survival plot of GL261 bearing *Rag2*$^{-/-}$ mice that were pre-treated with AAV-PHP.eB transducing sg*Anxa1* or *Rosa26* control under the GFAP promoter, as in Fig. 4l,m. (n = 8 mice per group, and p value from log rank; experiment replicated twice). Data are mean and error bars show ± SEM (**a, e**).

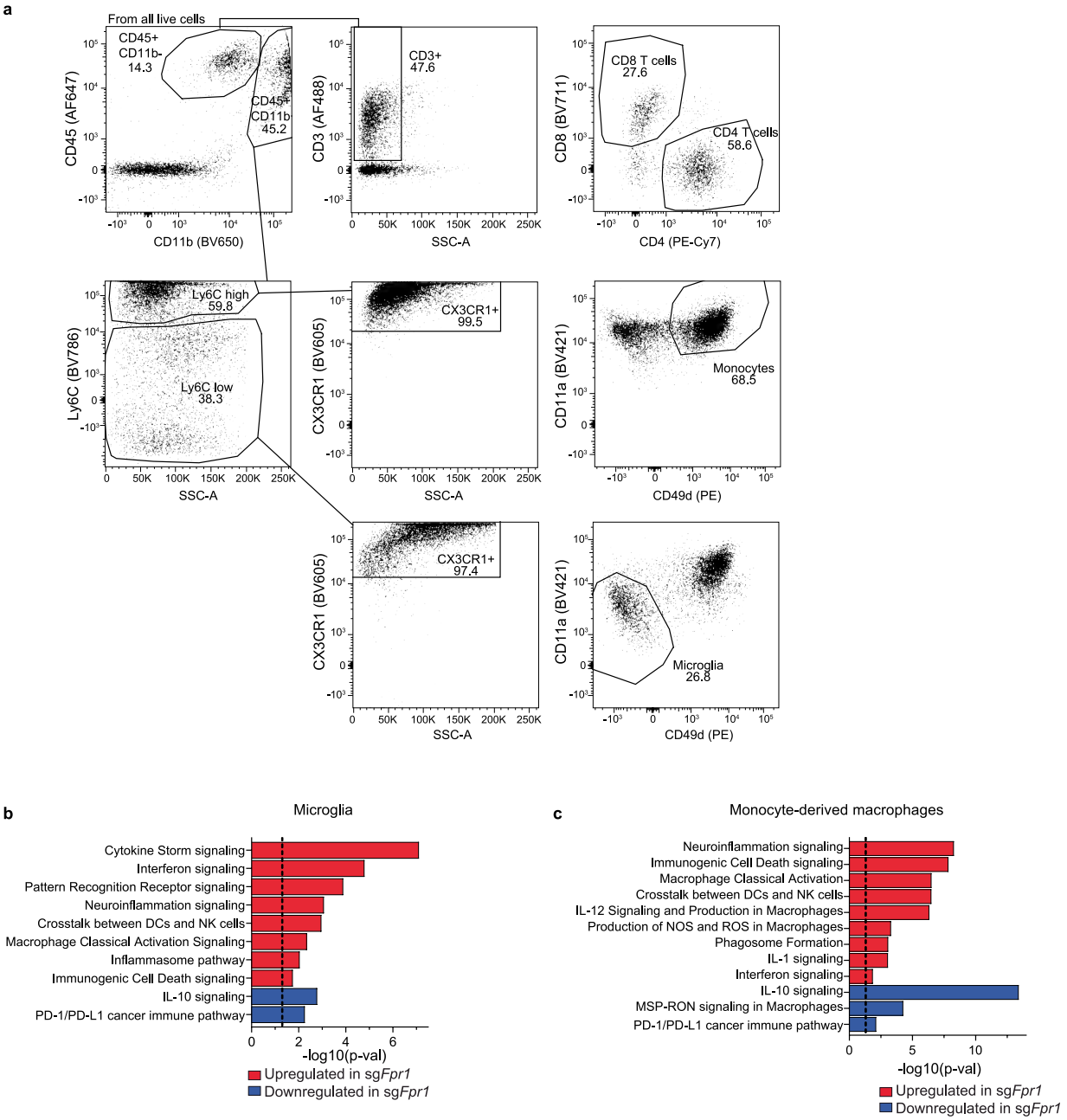

Extended Data Fig. 8 | Flow gating, TAM RNA-seq in GL261sg*Fpr1* and AAV PHP-eB-GFAP-sg*Anxa1*. (**a**) Flow cytometry gating scheme. (**b,c**) Ingenuity pathway analysis on microglia (b) and monocyte-derived macrophages (c), based on differential gene expression between sg*Fpr1* vs. sg Random GL261 bearing mice (n = 4 mice for sgRandom and n = 5 mice for sg*Fpr1* group).

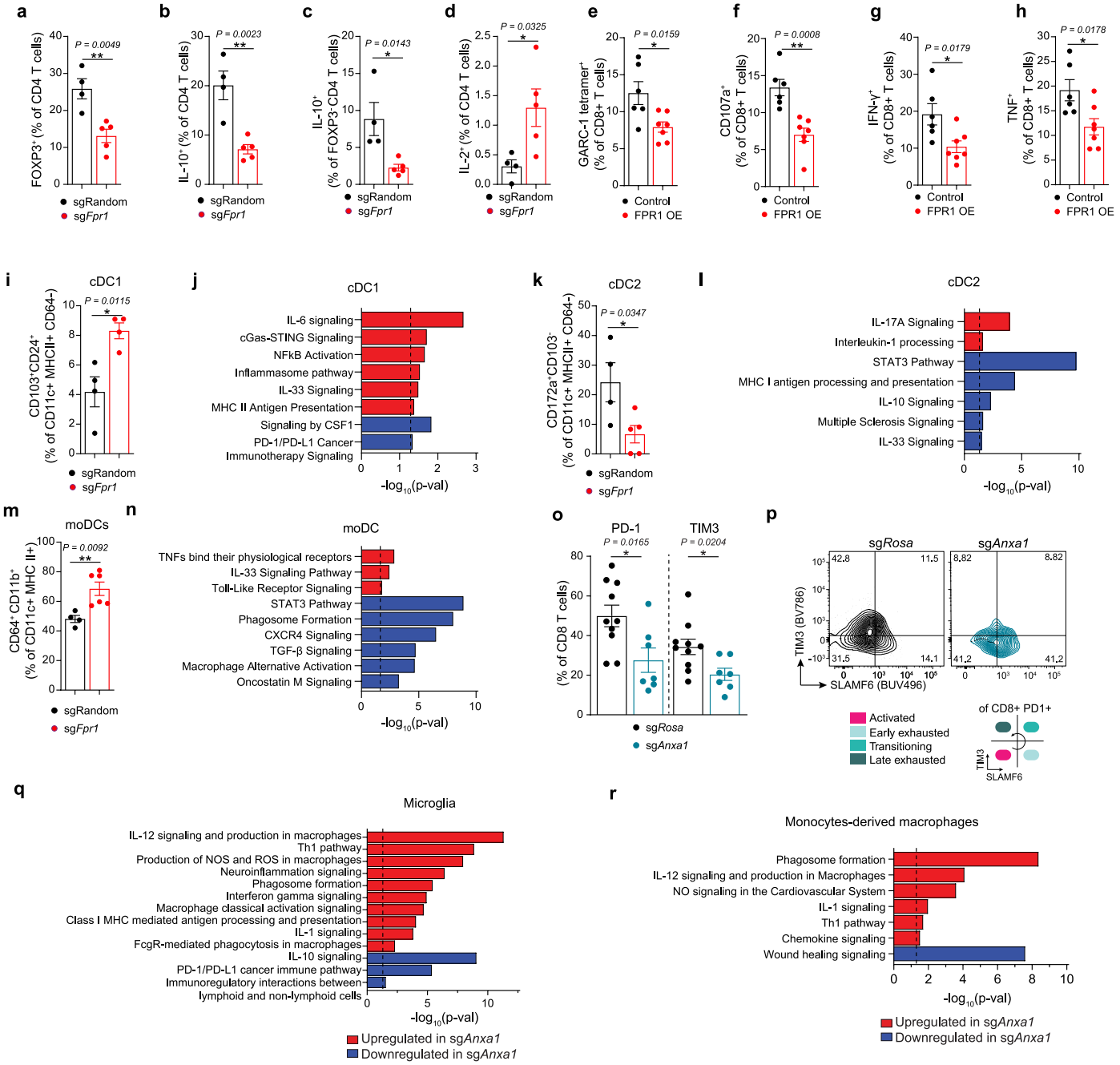

Extended Data Fig. 9 | Effect on T cells and DCs of *Fpr1* perturbation and overexpression in GL261 cells. (a-d) Analysis of CD4 T-cells in the presence or absence of GL261 cell inactivation of *Fpr1*. (a) FOXP3$^+$ CD4$^+$ T cells (n = 4 sgRandom and n = 5 *sgFpr1* mice), (b) IL-10$^+$ CD4$^+$ T cells (n = 4 sgRandom and n = 5 *sgFpr1* mice), (c) FOXP3$^-$IL-10$^+$ CD4$^+$ T cells (n = 4 sgRandom and n = 5 *sgFpr1* mice), and (d) IL-2$^+$ CD4$^+$ T cells were quantified (n = 4 sgRandom and n = 5 *sgFpr1* mice). **(e-h)** CD8 T cell suppression upon over-expression of FPR1 in GL261, including tetramer staining for GARC-1 (e; n = 6 control and n = 7 *Fpr1* OE mice) and CD107a (f; n = 6 control and n = 7 *Fpr1* OE mice), IFN-γ (g; n = 6 control and n = 7 *Fpr1* OE mice) and TNF (h; n = 6 control and n = 7 *Fpr1* OE mice). **(i-n)** Conventional (cDC) and monocyte-derived dendritic cell (moDC) quantification and gene expression analysis following GL261 cell inactivation of *Fpr1*, including cDC1 abundance (i; n = 4 mice per group), pathway analysis (j; n = 3 sgRandom and n = 3 sg*Fpr1* mice), cDC2 abundance (k; n = 4 sg Random and n = 5 sg*Fpr1* mice per group) and pathway analysis (l; n = 3 sgRandom and n = 3 sg*Fpr1* mice), and monocyte-derived DC (moDC) abundance (m; n = 4 sgRandom and n = 6 sg*Fpr1* mice) and pathway analysis (n; n = 3 sgRandom and n = 3 sg*Fpr1* mice). **(o, p)** Exhaustion markers of CD8 T cells from animals receiving *sgAnxa1* or *sgRosa* are shown (n = 10 for sg*Rosa* and n = 7 for sg*Anxa1*; *left, PD-1*, and right, TIM-3). (p) contour plot of exhaustion stages of CD8$^+$ T cells. **(q-r)**. Pathway analysis on microglia (q) and monocyte-derived macrophages (r) based on RNA-seq between mice transduced with AAV-PHP.eB sg*Anxa1* vs. sg*Rosa* followed by GL261-Luc2 implantation (n = 3 mice per group). All p values were from two-sided unpaired t-test. Data are mean and error bars show ± SEM **(a-i; k, m, o)**.

nature portfolio

Corresponding author(s): Francisco J. Quintana

Last updated by author(s): Apr 29, 2025

Reporting Summary

Nature Portfolio wishes to improve the reproducibility of the work that we publish. This form provides structure for consistency and transparency in reporting. For further information on Nature Portfolio policies, see our Editorial Policies and the Editorial Policy Checklist.

Statistics

For all statistical analyses, confirm that the following items are present in the figure legend, table legend, main text, or Methods section.

n/a	Confirmed
☐	☒ The exact sample size (*n*) for each experimental group/condition, given as a discrete number and unit of measurement
☐	☒ A statement on whether measurements were taken from distinct samples or whether the same sample was measured repeatedly
☐	☒ The statistical test(s) used AND whether they are one- or two-sided *Only common tests should be described solely by name; describe more complex techniques in the Methods section.*
☐	☒ A description of all covariates tested
☐	☒ A description of any assumptions or corrections, such as tests of normality and adjustment for multiple comparisons
☐	☒ A full description of the statistical parameters including central tendency (e.g. means) or other basic estimates (e.g. regression coefficient) AND variation (e.g. standard deviation) or associated estimates of uncertainty (e.g. confidence intervals)
☐	☒ For null hypothesis testing, the test statistic (e.g. *F*, *t*, *r*) with confidence intervals, effect sizes, degrees of freedom and *P* value noted *Give P values as exact values whenever suitable.*
☒	☐ For Bayesian analysis, information on the choice of priors and Markov chain Monte Carlo settings
☒	☐ For hierarchical and complex designs, identification of the appropriate level for tests and full reporting of outcomes
☐	☒ Estimates of effect sizes (e.g. Cohen's *d*, Pearson's *r*), indicating how they were calculated

Our web collection on statistics for biologists contains articles on many of the points above.

Software and code

Policy information about availability of computer code

Data collection	BD FACSDIVA (v.8.0.1)
Data analysis	DESeq2 (v4.3), Trim Galore (v0.6.5), Seurat package (v4.3), dittoSeq (v4.3), circlize (v0.4.16), ggplot2 (v3.5), EnhancedVolcano (v3.17), RStudio (v4.3.0) with R (v4.3.1), miloR (v1.8.1), GSEA (v4.3.2), MSigDB (v2023.1), QuPath (v0.3.2 with Java 16.0.2), GraphPad Prism 10 (v10.0.2), SPATA2 (v2.0.4), PantherDB (v17.0), Adobe Illustrator (v28.0), FlowJo (v10.9.0)

For manuscripts utilizing custom algorithms or software that are central to the research but not yet described in published literature, software must be made available to editors and reviewers. We strongly encourage code deposition in a community repository (e.g. GitHub). See the Nature Portfolio guidelines for submitting code & software for further information.

Data

Policy information about availability of data

All manuscripts must include a data availability statement. This statement should provide the following information, where applicable:

- Accession codes, unique identifiers, or web links for publicly available datasets
- A description of any restrictions on data availability
- For clinical datasets or third party data, please ensure that the statement adheres to our policy

Sequencing data have been deposited in GEO under the SuperSeries accession code Human data: GSE263612. Token: obmjyoiurfetxer.
Mouse single cell data: GSE263613. Token: mzodacysrtgpbin. Mouse bulk RNA seq data: All other data are available from the corresponding authors on reasonable request. Correspondence and request for materials should be addressed to F.J.Q. Publicly available datasets: scRNA-seq dataset from Couturier et al, 2022: https://github.com/kpetrecca/NeuroOncology2022.git; spatial transcriptomics based module datasets from Ravi, Will, Kuecklehaus et al., 2024: https://datadryad.org/

dataset/doi:10.5061/dryad.h70rxwdmj; Ivy Glioblastoma Atlas: http://glioblastoma.alleninstitute.org; TCGA/GLASS: http://www.cbioportal.org; GRCh38 reference genome: https://ftp.ensembl.org/pub/release-113/fasta/homo_sapiens/dna/

Field-specific reporting

Please select the one below that is the best fit for your research. If you are not sure, read the appropriate sections before making your selection.

☒ Life sciences ☐ Behavioural & social sciences ☐ Ecological, evolutionary & environmental sciences

For a reference copy of the document with all sections, see nature.com/documents/nr-reporting-summary-flat.pdf

Life sciences study design

All studies must disclose on these points even when the disclosure is negative.

Sample size	No statistical methods were used to predetermine sample sizes. Sample sizes are similar to those used in the field, as previously reported: Lee HG et al, Nature 2024 Sanmarco and Wheeler et al. Nature 2021 Wheeler et al. Nature 2020, Wheeler et al. Nature 2019, Chao et al. Cell 2019, Rothhammer et al. Nature 2018, Rothhammer et al. Nature Medicine 2016, Mayo et al. Nature Medicine 2014.
Data exclusions	Formal outlier tests in Prism (9.2.0) were used to exclude outlying datapoints, which was pre-established and similar to exclusion criteria described in recent publications: (Vujkovic-Cvijin et al., Nature 2020; Ballesta et al., Nature 2020; Lukonin et al., Nature 2020; Badimon et al., Nature 2020; Wheeler et al., Nature 2020; Wheeler et al., Cell 2019; Hur et al., Nature 2020; Sahin et al., Nature 2020).
Replication	To ensure replication, all deep sequencing data were repeated in 3-5 mice per group per timepoint. For in vitro and in vivo experiments, experiments were repeated at least twice, with consistent results.
Randomization	All samples were randomly allocated into treatment groups.
Blinding	Experimenters were blinded to treatment during survival study monitoring. Similarly, during data processing of all sequencing data, experimenters were blinded to condition. Otherwise, blinding was not performed, such as during in vitro experiments, where experimenters were required to know the conditions of each well.

Reporting for specific materials, systems and methods

We require information from authors about some types of materials, experimental systems and methods used in many studies. Here, indicate whether each material, system or method listed is relevant to your study. If you are not sure if a list item applies to your research, read the appropriate section before selecting a response.

Materials & experimental systems

n/a	Involved in the study
☐	☒ Antibodies
☐	☒ Eukaryotic cell lines
☒	☐ Palaeontology and archaeology
☐	☒ Animals and other organisms
☐	☒ Human research participants
☐	☒ Clinical data
☒	☐ Dual use research of concern

Methods

n/a	Involved in the study
☒	☐ ChIP-seq
☐	☒ Flow cytometry
☒	☐ MRI-based neuroimaging

Antibodies

Antibodies used

Antibodies used for T-cell analysis were: BUV496 anti-SLAMF6 (BD Biosciences, 750046), BUV563 anti-CD11b (BD Biosciences, 741242), BUV661 anti-CD45 (BD Biosciences, 612975), BUV737 anti-PD-1 (BD Biosciences, 749306), BUV805 anti-LAG-3 (BD Biosciences, 748540), BUV650 anti-CD3 (BD Biosciences, 740530), BV711 anti-TIGIT (BD Biosciences, 744214), BV750 anti-TNF (BD Biosciences, 566365), BV786 anti-TIM3 (BD Biosciences, 747621), FITC anti-CD8a (Biolegend, 100804), PE anti-CTLA4 (Biolegend, 106306) or BV421 anti-CTLA4 (Biolegend, 106312), PE/Dazzle 594 anti-IL-10 (Biolegend, 505034), PE/Cy5 anti-IL2 (Biolegend, 503824), PE/Cy7 anti-CD4 (Biolegend, 100422), AF700 anti-CD39 (Invitrogen, 56-0391-82), APC/Cy7 anti-IFNγ (BD Biosciences, 561479). GL261-specific CD8+ T cells were stained with an APC-conjugated H-2D(b) tetramer loaded with GARC-177-85 peptide (AALLNKLYA) (NIH Tetramer Core) was used.
The anti-FPR1 blocking antibody was from R&D Systems (clone 350418, catalog MAB3744; lot XSU0422112).
Antibodies used for sorting were: BV421 anti-CD11a (BD Biosciences, 740020), BV605 anti-CX3CR1 (Biolegend, 149027), BV650 anti-CD11b (BD Biosciences, 563402), BV711 anti-CD8a (BD Biosciences, 752634), BV785 anti-Ly6C (Biolegend, 128041), FITC anti-CD3 (Biolegend, 100204), PE/Cy7 anti-CD4 (Biolegend, 100422), APC anti-CD45 (Thermo Fisher Scientific, 17-0451-83), APC/Cy7 anti-CD49d (Biolegend, 103635).
Immunofluorescence staining of mouse tissue and human cells (all antibodies cross react with both species): ASC (Adipogen; AL177; 1:100), cleaved IL-1B (Thermo Fisher Scientific; PA5-105048 1:200), and NFkB (Cell Signaling Technology, Clone D14E12; 1:100). pMLKL (Cell Signaling Technology; 1:100), GFAP (Abcam ab4674: 1:500), Luciferase (BioRad; MCA2076; 1:100), and DAPI (Sigma

Aldrich: 1:1,000). Secondary antibodies were used at 1:1,000 and were: donkey anti-rabbit Alexa Fluor 647 (Invitrogen A31573), donkey anti-chicken Alexa Fluor 594 (Invitrogen A21203), goat anti-chicken Alexa Fluor 488 (Invitrogen A78948), and donkey anti-rabbit Alexa Fluor 488 (Invitrogen A21206).
Immunofluorescence staining of human tissue using the 4i method: Antibodies used in cycle 1 used were: GFAP (DAKO (Zo334, 1:1000), Iba1 (Synaptic Systems, 234308); cycle 2 antibodies were ANXA1 (abcam ab214486: 1:2000), FPR1 (Abcam ab113531, 1:100); cycle 3 antibody was FPR3 (BioTechne, MAB3896, 1:500); cycle 4 antibody was FPR2 (Santa Cruz, sc-57141, 1:200), and cycle 5 antibodies were EFGRvIII (Biozol, 31-1305-00, 1:100), GFAP (DAKO, Z0334, 1:100), and hematoxylin.

Validation

All antibodies were commercial in origin and validated by the company. Specifically, BioLegend (https://www.biolegend.com/nl-nl/reproducibility), Abcam (https://www.abcam.com/primary-antibodies/how-we-validate-our-antibodies), BD Biosciences, Miltenyi (https://www.miltenyibiotec.com/US-en/resources/macs-academy/live-webinars/antibody-validation-for-reproducible-flow-cytometry-analysis.html#gref), Thermo Fisher (https://www.thermofisher.com/us/en/home/life-science/antibodies/invitrogen-antibody-validation.html), R&D Systems (https://www.rndsystems.com/quality/antibodies-built-for-reproducibility#:~:text=R%26D%20Systems%C2%AE%20takes%20rigorous%20steps%20towards%20antibody%20validation%20and%20reproducibility.&text=By%20developing%20and%20testing%20our,100%25%20guarantee%20for%20our%20products.), and Millipore (https://www.emdmillipore.com/US/en/life-science-research/antibodies-assays/antibodies-overview/Antibody-Development-and-Validation/cFOb.qB.8McAAAFOb64qQvSS,nav), purify antibodies from cell line supernatant using affinity chromatography followed by validation using proper negative and positive controls in functional assays, relevant for all antibodies used for flow cytometry and immunostaining. Additionally, co-authors reviewed staining properties with positive and negative controls to ensure no non-specific staining (regarding subcellular location by microscopy, appropriate co-staining with other markers).

Eukaryotic cell lines

Policy information about cell lines

Cell line source(s)	GL261-luc2, CT-2A-Luc2 (Caliper Life Sciences); NIH-3T3 (ATCC); BT 1018, BT482, BT145 (Dana-Farber Cancer Institute Center for Patient Derived Models (available at models@dfci.harvard.edu).
Authentication	cell lines were authenticated by their suppliers by RNA-seq, histological analysis, STR, and pathogen PCR panels (eg CLEAR).
Mycoplasma contamination	Cells tested negative for mycoplasma by their suppliers and low passage (<3 passages) stocks were banked for experimental use.
Commonly misidentified lines (See ICLAC register)	None.

Animals and other organisms

Policy information about studies involving animals; ARRIVE guidelines recommended for reporting animal research

Laboratory animals	Mice were housed 2-5 animals per cage under a standard light cycle (12h light/dark) (lights on from 7am to 7 pm) at 20-23°C and humidity (~50%) with ad libitum access to water and food. WT C57Bl/6J (The Jackson Laboratory, #000664); Male and female mice were used. Mice were 8-12 weeks old when used for experiments.
Wild animals	The study did not involve wild animals
Field-collected samples	The study did not involve samples collected from the field.
Ethics oversight	Brigham and Women's Hospital IACUC.

Note that full information on the approval of the study protocol must also be provided in the manuscript.

Human research participants

Policy information about studies involving human research participants

Population characteristics	Human GBM samples were analyzed from n=31 GBM patients and n=4 control tissue. Covariate information is included in tables S1, S2, and Supplementary Data 3. Covariate data from TCGA/GLASS are available at cbioportal.org.
Recruitment	All patients were recruited through the Department of Oncologic Pathology at Dana Farber Cancer Institute. Informed consent from both the patients and the family was obtained. Patients were chosen based on a clinical diagnosis of GBM, thus a self-selection bias is not relevant.
Ethics oversight	Resected GBM and healthy brain tissue samples were collected from GBM patients with full ethical approval and informed consent as approved by the Department of Oncologic Pathology at Dana Farber Cancer Institute.

Note that full information on the approval of the study protocol must also be provided in the manuscript.

Clinical data

Policy information about clinical studies

All manuscripts should comply with the ICMJE guidelines for publication of clinical research and a completed CONSORT checklist must be included with all submissions.

Clinical trial registration	*Provide the trial registration number from ClinicalTrials.gov or an equivalent agency.*
Study protocol	*Note where the full trial protocol can be accessed OR if not available, explain why.*
Data collection	*Describe the settings and locales of data collection, noting the time periods of recruitment and data collection.*
Outcomes	*Describe how you pre-defined primary and secondary outcome measures and how you assessed these measures.*

Flow Cytometry

Plots

Confirm that:

☒ The axis labels state the marker and fluorochrome used (e.g. CD4-FITC).

☒ The axis scales are clearly visible. Include numbers along axes only for bottom left plot of group (a 'group' is an analysis of identical markers).

☒ All plots are contour plots with outliers or pseudocolor plots.

☒ A numerical value for number of cells or percentage (with statistics) is provided.

Methodology

Sample preparation	Mouse CNS cells: Anesthetized mice were perfused with 20 mL cold PBS. The brain was minced and enzymatically dissociated for 20 min, 37°C and 100 rpm shaking in a solution containing 0.66 mg/mL Papain (Sigma-Aldrich, #P4762) in HBSS w/o Mg/Ca (Thermo Fisher Scientific, 14175095), followed by a second incubation at the same conditions with equal volume of DMEM supplemented with Collagenase D (Roche, #11088858001) and DNase I (Thermo Fisher Scientific, #90083) in the concentration of 0.66 mg/mL and 8 U/mL respectively. Using a 10mL serological pipette, the suspension was dissociated and filtered through a 70 µm cell strainer (Fisher Scientific, #22363548) into a 50 mL tube. After centrifugation at 600xg for 5 min, the pellet was resuspended in 10mL of a solution containing 30% Percoll (GE Healthcare Biosciences) in PBS. Following gradient centrifugation for 25 min at 600xg with lowest acceleration and deceleration speeds, the layer of myelin accumulating at the top was aspirated. The cell pellet was washed with PBS and used for downstream applications. Mouse splenic cells: Mouse spleens were dissected out of anesthetized mice prior to cardiac perfusion, mechanically mashed through 70µm nylon strainers (Thermo Fisher Scientific, 22-363-548) by use of a syringe plunger, and washed with HBSS w/o Mg/Ca (Thermo Fisher Scientific, 14175095). Next, spleen tissue was incubated in 1mL ACK Lysis Buffer (Gibco, A10492) for 5 min at 4°C to lyse red blood cells, washed in HBSS, centrifuged at 500 xg and resuspended in PBS with 0.5% BSA (Sigma-Aldrich, A3294-100G) and 2mM EDTA (VWR, E177-100ML) for downstream applications.
Instrument	BD FACSAria IIu or BD Facs Symphony A5.
Software	BD FACSDIVA (v8.0.1)
Cell population abundance	Sorting was performed with "Purity" settings, thus purity is >95%. Abundance is reported in figures where relevant.
Gating strategy	Gating strategies are shown for each flow cytometry experiment

☒ Tick this box to confirm that a figure exemplifying the gating strategy is provided in the Supplementary Information.